

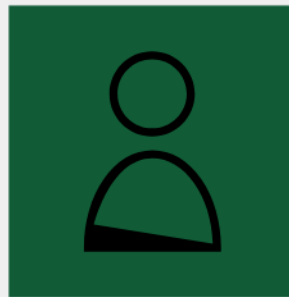
Wiley Analytical Science

The Current State of Reconstruction Technologies for 3D X-ray Microscopy including Algorithmic Innovation for AI-based Recovery

April 26, 10:00am - 11:00am EDT

Many properties can only be fully understood in 3D, such as porosity and tortuosity in porous materials, network connection maps in neuroscience, or mechanical properties in 3D additively manufactured structures. X-ray microscopy provides a unique method to image samples non-destructively in 3D across a wide range of materials and life sciences.

Watch this session during the WAS Virtual Conference:



Nicolas Guenichault, Ph.D.



Dr. Stephen T. Kelly, Ph.D.

Register Now

This talk is sponsored by



Time-Resolved Terahertz Spectroscopy Studies on 2D Van der Waals Materials

Peng Han, Xinke Wang, and Yan Zhang*

Owing to the fascinating and technologically useful electronic and optical properties, 2D van der Waals (vdW) materials are viewed as the key component for the next-generation optoelectronic, photovoltaic, and nanoelectronic devices. Fully understanding the ultrafast carrier dynamics in 2D vdW materials is essential to study the fundamental physics and realize potential applications. Time-resolved terahertz (THz) spectroscopy is a powerful tool used to investigate the ultrafast carrier dynamics and transport properties in semiconducting materials. In recent years, the time-domain THz spectroscopy measurements, with or without photoexcitation on samples, are widely used to investigate the carrier dynamics of 2D vdW materials. A brief summary on the recent progress of time-domain THz spectroscopy studies on ultrafast dynamics processes is provided. These include exciton formation and relaxation processes in semiconducting 2D materials, the relaxation of hot electrons in graphene layers, the conductivity of 2D materials modulated by femtosecond laser pulses, and their related physical properties. Finally, the physical properties of 2D vdW materials observed using the time-domain THz spectroscopy approach are highlighted and the future challenges for time-resolved THz spectroscopy investigations on 2D vdW materials are presented.

bulk diamond with tetrahedral structure, graphite is another allotrope of carbon with layered hexagonal lattice structure. In single- or few-layer graphite, which is also referred to as graphene, carbon atoms are strongly coupled by covalent bonds in plane and weakly coupled through van der Waals (vdW)-like interactions in layered direction;^[2,3] such 2D-layered atomic crystals are commonly referred as “2D vdW materials.”^[3–5] Following the discovery of graphene, insulating 2D-layered hexagonal boron nitride (h-BN) was initially predicted in theory and then synthesized in experiments.^[6,7] Soon after the discovery of semimetallic graphene and the insulating h-BN, semiconducting-layered 2D vdW materials, for example, transition-metal dichalcogenides (TMDs), monochalcogenides, black phosphorus (BP), 2D oxides, and transition metal carbides/carbon nitrides (MXenes) were synthesized by using different physical or chemical synthesis approaches such as mechanical exfoliations, wet-chemical synthesis, and chemical vapor-phase depositions.^[4,5,8–14] To date, more than 500 types of 2D vdW materials have been synthesized in laboratories.

Owing to their high in-plane charge carrier mobility^[15] and a wide range of energy bandgaps varies from tens of millielectron volts (meV) to few electron volts (eV),^[16,17] semiconducting 2D materials have been viewed as a key component for the next-generation optoelectronic devices.^[18–22] In addition to the high carrier mobility and wide spectral range, intriguing spin-valley physics, induced by the strong spin-orbit coupling and band structures,^[23–25] strong Coulomb interactions, which originate from the strict out-of-plane quantum confinement and reduced dielectric screenings,^[26,27] along with the large exciton-binding energies enrich the physical properties of photoexcited quasiparticles (e.g., exciton, trion, and biexciton) in 2D vdW semiconductors. In addition to these exciting physical properties, another attractive characteristic of 2D vdW materials is to stack them into structures that are constructed through vdW interactions, without introducing defects or lattice distortions at the interfaces. The unique physical properties along with the vdW interlayer interaction allow for the fabrication of high-performance devices with extremely fast responses, such as high-mobility GHz-frequency field-effect transistors,^[28,29] fast response phototransistors,^[30] and extremely sensitive chemical detectors.^[31]

1. Introduction

Dimensionality is the dominated quantity to describe the quantum confinement effects on nanomaterials. In addition to the well-documented low-dimensional nanostructures, for example, from 2D quantum wells or nanoflakes to 1D nanowires or quasi-1D nanotubes, and eventually to 0D nanoclusters or quantum dots, the discovery of single-layer graphene in 2004 has fundamentally changed the landscape of materials science, owing to its unique physical properties and stable single-atom or single-polyhedral thickness.^[1,2] In contrast to

Dr. P. Han, Dr. X. Wang, Prof. Y. Zhang
 Department of Physics
 Beijing Key Lab for Metamaterials and Devices
 Key Laboratory of Terahertz Optoelectronics
 Ministry of Education
 Beijing Advanced Innovation Center for Imaging Theory and Technology
 Capital Normal University
 Beijing 100048, China
 E-mail: yzhang@cnu.edu.cn

The ORCID identification number(s) for the author(s) of this article can be found under <https://doi.org/10.1002/adom.201900533>.

DOI: 10.1002/adom.201900533

Recent developments in 2D devices with a fast optoelectronic response have resulted in further requirements on understanding the fundamental physics of photoexcited charge carriers and their interactions with lattice vibrations and unexcited electrons within the time scale of femtoseconds to picoseconds.^[32] To investigate such ultrafast dynamic processes of free charge carriers or quasiparticles and their interactions with lattice vibrations and unexcited cold electrons in 2D vdW materials, such as rapid exciton-exciton scattering, charge-transfer process, exciton-phonon interaction, and formation and recombination processes of excitons, tremendous efforts have been made from both theoretical and experimental aspects in recent years. In theory, thanks to the recent developments of the ab initio algorithm and highly efficient large-scale parallel computing techniques, accurate descriptions of the ultrafast carrier and lattice dynamics have become possible in 2D vdW materials. During the past 5 years, ultrafast energy and charge carrier transfer processes in excited monolayer MoSe₂ and relaxation pathways of photoexcited charge carriers in few-layer MoS₂ have been studied by performing ab initio time-dependent density functional theory (DFT) calculation and nonadiabatic molecular dynamics simulation, respectively.^[32,33] In experiment, measurements of the absorption and emission spectra, lattice vibrational modes, energy band structures, and photoconductivity of 2D vdW materials have been performed by using photoluminescence (PL) spectroscopy,^[34,35] Raman spectroscopy,^[36,37] angle-resolved photoemission spectroscopy,^[38,39] optical pump-probe measurements, and optical pump-terahertz (THz) probe measurements.^[40–42] These studies have enhanced the understanding of the physical properties of 2D vdW materials.

Among the above experimental approaches, the time-resolved THz spectroscopy technique possesses numerous advantages, which include sensitivity to the response of charge carriers, covers the energy ranges of exciton-binding energy, intraband transitions, and phonon resonance, and the ability to extract the frequency-resolved complex conductivity and dielectric response. The measured THz response data along with the analysis using classical Drude response model further provide information of the carrier mobility and charge density in the time or frequency domain. The properties of time-resolved THz spectroscopy technique enable it to be used as a powerful tool to reveal the fundamental physics in ultrafast dynamics of charge carriers in materials.^[43] By extracting the time- or frequency-resolved complex conductivity and dielectric response from the detected ultrashort coherent electromagnetic pulses, the formation and decay processes of photoexcited charge carriers and excitons, which are the photoinduced positive or negative conductivity in both semiconducting and semimetallic 2D vdW materials, have been well studied using the time-domain THz spectroscopy technique.^[43]

This review explores the time-resolved THz spectroscopy studies on the ultrafast dynamics and transport properties of charge carriers in 2D vdW materials. In the beginning of the review, we give a brief description of the time-resolved THz spectroscopy approach, which covers the technical details of the time-resolved THz spectroscopy setup and how to extract material properties from the measured data. We then focus on the fabrication and the physical characteristics, such as electronic



Yan Zhang is currently a Professor in the Department of Physics, Capital Normal University, China. He is the Dean of Beijing Key Lab for Metamaterials and Devices. He received his bachelor's and master's degrees from Harbin Institute of Technology, and his Ph.D. degree from the Institute of Physics, Chinese Academy of Science. His research interests include terahertz imaging and spectroscopy, surface plasmonic optics, and optical information processing. He is a fellow of The Optical Society (OSA).

structures and optical properties, of 2D-layered vdW materials in Section 3. In Sections 4 and 5, the THz time-domain spectroscopy (THz-TDS) studies for the evaluation of photoexcited charge carriers and the conductivity in 2D vdW materials will be discussed, respectively. For an evaluation of photoexcited carriers, we will discuss the formation and relaxation processes of excitons in 2D semiconductors and of photoexcited hot electrons in layered graphene. Regarding the conductivity, we will focus on the properties of frequency-resolved complex conductivity in 2D vdW materials with and without photoexcitation. A brief summary, with an outlook of time-domain THz spectroscopy studies on 2D vdW materials, will be given in Section 6.

2. Time-Resolved THz Spectroscopy

2.1. THz Radiation: Source and Detection

THz radiation is a type of sub-millimeter-wavelength electromagnetic radiation with low photon energy (4.2 meV for 1 THz) and has the potential to penetrate nonpolar material. To generate and detect the THz signal in time-domain spectroscopy, enormous attentions have been paid on the ultrafast optics since the beginning of 1990s.^[44–46] In the state-of-the-art time-resolved THz spectroscopy technique, the femtosecond lasers are widely used to excite THz electromagnetic waves and the THz signals are primarily detected by using electric field-resolved measurements. Nonlinear optical processes and the photoconductivity approach are the two major techniques to excite and detect THz radiation based on femtosecond laser sources.^[43]

A nonlinear optical process is a nonresonant physical process. In this process, THz radiation with frequency much lower than the intense laser is generated when the intense laser propagates through a crystal with noncenter symmetry. In principle, the bandwidth of THz radiation generated through a nonlinear optical process is only confined by the laser excitation pulse width and the phonon absorption window of the nonlinear optical media. The band ranges of THz emission generated

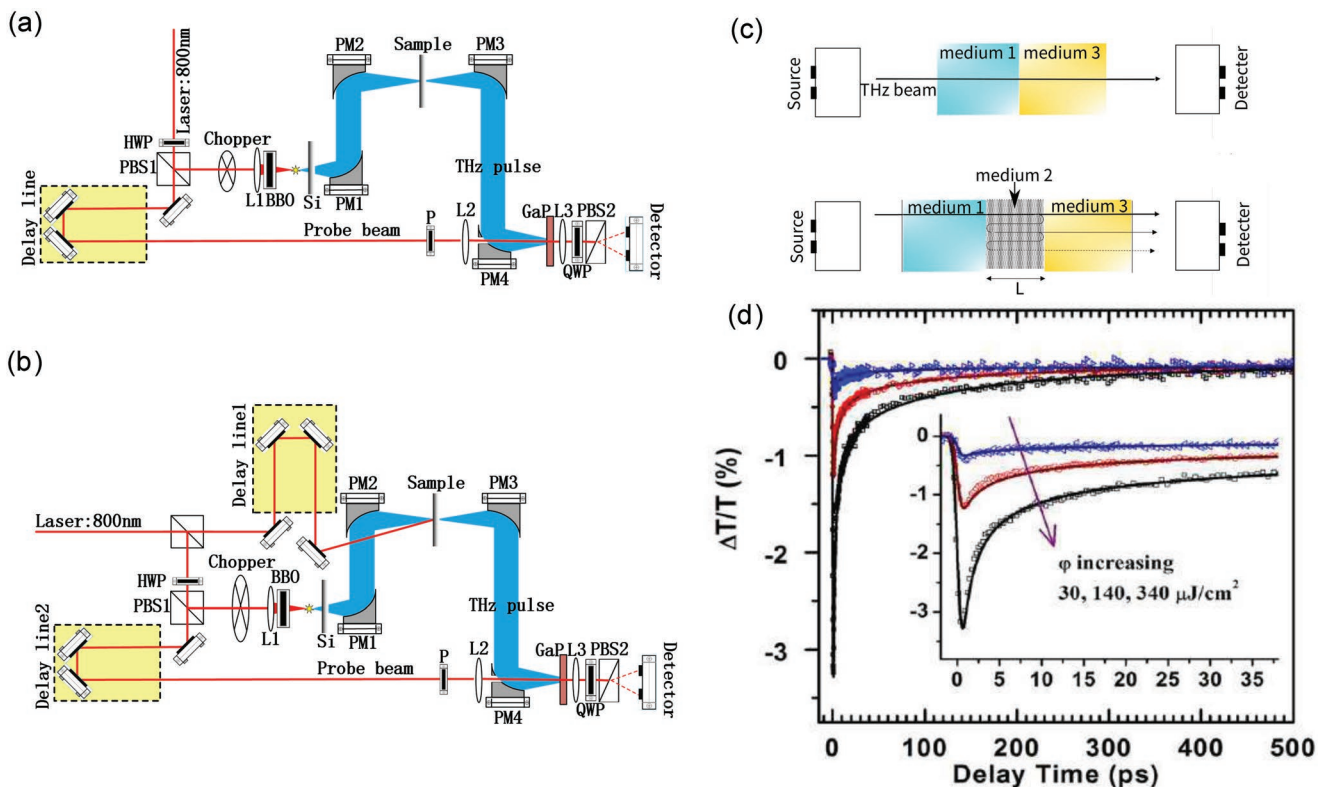


Figure 1. a) Schematic representation of a THz time-domain spectroscopy setup. b) Schematic representation of an optical pump-THz probe spectroscopy setup. HWP: half wavelength plate, PBS, polarization beam splitter, L: lens, Si: silicon wafer, PM: parabolic mirror, P: polarizer, QWP: quarter wavelength plate. c) Schematic representation of the optical path of the THz beam between the transmitting and receiving antennas without (upper diagram) and with (lower diagram) a sample inserted between media 1 and 3. d) Optical pump-THz probe studies on the ultrafast dynamic process of photoexcited charge carriers in few-layer MoS₂ material. The solid lines are the fitting curves. Inset: relaxation dynamics up to 40 ps. d) Reproduced with permission.^[57] Copyright 2015, American Chemical Society.

using standard Ti:sapphire laser with commonly-used nonlinear optical crystals ZnTe, GaP, and GaSe are 0–3, 2–7, and 8–40 THz, respectively.^[47–49] In addition to the nonlinear optical crystals, plasmas are also widely used as nonlinear mediums to generate broadband THz radiation. Owing to the lack of phonon absorption, no spectral gaps appear in the band of THz radiations generated by a plasma.^[50] As an alternative method, THz radiation can be generated based on photoconductivity. The working principle of a photoconductive antenna on the photoconductivity is a resonant process. In this process, charge carriers are excited from the valence band to the conduction band by the femtosecond laser pulse. The photogenerated charge carriers are then drafted by an external or build-in field to form photocurrent. This leads to the emission of THz electromagnetic transient into the free space as a THz photoconductive antenna.^[51–53]

As an opposite process, the detection of a THz electromagnetic transient can be achieved either based on a nonlinear optical process or by using the photoconductivity approach.^[54] In the nonlinear optical process, the linear electro-optic (EO) effect of semiconductor crystal produces a birefringence in the EO crystal under a bias electric field induced by the THz radiation. This birefringence rotates the probe beam polarization and leads to the change of probe beam intensity after transmitting

through the EO crystal.^[55] The time-resolved waveform of THz transient is achieved by scanning the THz pulse-probe beam time delay. Compared with the nonlinear optical process, THz detection by the photoconductive antenna approach is based on the following working principle. When an optical and a THz pulses simultaneously enter into the semiconductor detector, photoexcited charge carriers are accelerated by the THz pulse to form a photocurrent. THz electromagnetic pulse is therefore measured from the photoinduced current.

2.2. THz Time-Domain Spectroscopy Setup

Figure 1a schematically illustrates a widely used THz-TDS system. As indicated in Figure 1a, sub-picosecond laser pulses are required to generate the THz pulses and to detect the THz transient. The ultrashort incident laser pulses with a wavelength of 800 nm are generated by a Ti:sapphire mode-locked laser amplifier. The incident laser beam is separated into two portions by a beam splitter (BS), one is used to generate the THz radiation while the other is used to probe the transmitted THz signal. By passing through the THz emitter, which could be a non-centrosymmetric crystal, or a barium borate (BBO) crystal with a silicon wafer, or a photoconductive antenna dependent

on different approaches, the THz pulse is generated and subsequently focused on the sample by propagating through metallic parabolic mirrors (PM1–PM4) and silicon lens. After traveling through a mechanical delay stage and passing through a polarizer (P), the probe beam is collinear with the transmitted THz pulse and then accepted by the detector. Details of THz-TDS systems have been provided in previous reviews.^[58–60]

2.3. Optical Pump–THz Probe Spectroscopy Setup

The optical pump–THz probe spectroscopy system can be easily converted from a standard THz-TDS system by establishing an optical pump path. As illustrated in Figure 1b, the pump beam and the laser beam for the THz-TDS system are derived from the same femtosecond mode-locked laser. The central wavelength of the pump pulse can be halved to 400 nm by traveling through a nonlinear optical BBO crystal or tuned to various wavelengths by passing through an optical parametric amplifier (OPA). To adjust the pump–probe delay time, a stage is introduced into the pump path as the optical delay line.

2.4. Analysis of Measured Data

The working principle of a THz-TDS setup is to detect THz electromagnetic transients with a sub-picosecond time resolution. To characterize the time- and frequency-resolved material properties, measurements of electromagnetic transient with [$E_{\text{sam}}(t)$] and without [$E_{\text{ref}}(t)$] a sample in place are needed. Measurements of $E_{\text{sam}}(t)$ are usually divided into two types, the reflection and transmission approaches, depending on detecting the reflected or transmitted THz electromagnetic transients. In the following sections, we will discuss how to extract material properties from the transmitted THz transients. Analysis of the reflected THz transients can be found elsewhere,^[61] and will not be described in this review.

2.4.1. Complex Refractive Index and Dielectric Functions

In the linear response regime, the dielectric response of a material is characterized by using a frequency-resolved complex dielectric function $\tilde{\epsilon}(\omega) = \epsilon_1(\omega) + i\epsilon_2(\omega)$, which is involved with the complex refractive index $\tilde{n}(\omega)$ through the relation $\tilde{\epsilon}(\omega) = \tilde{n}^2(\omega)$.^[62] To extract the frequency-resolved material properties, the measured time-domain electric field waveforms are transformed into frequency-domain as $E_{\text{ref}}(\omega)$ and $E_{\text{sam}}(\omega)$ through the Fourier transform. The frequency-resolved transmission $T(\omega)$ is therefore written as

$$T(\omega) = \frac{E_{\text{sam}}(\omega)}{E_{\text{ref}}(\omega)} \quad (1)$$

In the general case, the 2D material sample is normally composed of a layered 2D vdW material lying on a dielectric substrate. The optical path of the THz beam in a THz-TDS measurement is schematically illustrated in Figure 1c. In Figure 1c, the protective layer, a sample of the 2D material,

and the dielectric substrate are referred to as media 1, 2, and 3, respectively. The thickness of the 2D material sample is set as L . To analyze the transfer matrix elements of this system, it is assumed that i) the plane wave impinges into the sample with a normal incidence, and ii) THz beam is linearly polarized with its polarization parallel to the optical axis of the sample. Based on the above assumptions, the transfer matrix of the transmitted THz wave is written as^[56]

$$S_{\text{sam}}(\omega) = \eta(\omega) T_{12}(\omega) P_2(\omega, L) T_{23}(\omega) M_{\text{FP}}(\omega) E(\omega) \quad (2)$$

where $E(\omega)$ denotes the electric field of THz wave emitted from the THz generator, $P_2(\omega, L)$ is the propagation coefficient in medium 2 over a distance L , $T_{ab}(\omega)$ denotes the transmission coefficient from medium a to medium b , and $M_{\text{FP}}(\omega)$ is the summation of the backward and forward reflections in the sample (referred to as Fabry–Pérot (FP) effect) respectively. The $\eta(\omega)$ term in Equation (2) includes all of the reflection, transmission, and propagation coefficients of the media. Similar to Equation (2), the transfer matrix without a sample is written as

$$S_{\text{ref}}(\omega) = \eta(\omega) T_{13}(\omega) P_{\text{air}}(\omega, L) E(\omega) \quad (3)$$

Using the transfer matrices $S_{\text{sam}}(\omega)$ and $S_{\text{ref}}(\omega)$, the complex transmission coefficient is further written as^[56]

$$T(\omega) = \frac{S_{\text{sam}}(\omega)}{S_{\text{ref}}(\omega)} = \frac{2\tilde{n}_2(\tilde{n}_1 + \tilde{n}_3)}{(\tilde{n}_2 + \tilde{n}_1)(\tilde{n}_2 + \tilde{n}_3)} \exp\left[-i(\tilde{n}_2 - \tilde{n}_{\text{air}})\frac{\omega L}{c}\right] M_{\text{FP}}(\omega) \quad (4)$$

with the FP term

$$M_{\text{FP}}(\omega) = \frac{1}{1 - \left(\frac{\tilde{n}_2 - \tilde{n}_1}{\tilde{n}_2 + \tilde{n}_1}\right) \left(\frac{\tilde{n}_2 - \tilde{n}_3}{\tilde{n}_2 + \tilde{n}_3}\right) \exp\left(-2i\tilde{n}_2\frac{\omega L}{c}\right)} \quad (5)$$

where c is the speed of light in vacuum, and $\tilde{n}_a = n_a(\omega) - i\kappa_a(\omega)$ denotes the complex refractive index of medium a .

In principle, the values of complex refractive index \tilde{n}_2 can be obtained via solving Equation (4) using the measured complex transmission coefficient given in Equation (1). Unfortunately, it is difficult to solve the complex refractive index from Equation (4) directly using either analytical or numerical algorithms.^[56,63] Usually, the thickness of a typical layered 2D material sample is approximately from few to tens of nanometers. Since the thickness of 2D vdW sample is much shorter than the wavelength of THz radiation, the FP term $M_{\text{FP}}(\omega)$ can be safely removed from Equation (4). Nevertheless, there is still no analytical solution to Equation (4) even with $M_{\text{FP}}(\omega) = 1$. To derive the complex refractive index, many approximations have been applied to Equation (4). For metallic 2D materials with a high refractive index $n_{\text{sam}} \gg n_{\text{sub}}$, such as layered graphene, Equation (4) can be approximately written in a commonly used thin-film expression without losing too much accuracy^[64,65]

$$T(\omega) = \frac{1 + \tilde{n}_{\text{sub}}}{1 + \tilde{n}_{\text{sub}} + Z_0\sigma(\omega)L} \exp\left[i(\tilde{n}_{\text{sub}} - 1)\frac{\omega\Delta L}{c}\right] \quad (6)$$

where Z_0 is the free space impedance, ΔL is the thickness of the sample comparing to the refereed substrate, and $\sigma_1(\omega) = 2n(\omega)\kappa(\omega)\omega\epsilon_0$ is the real part of the photoconductivity in sample with the vacuum permittivity ϵ_0 .

Alternatively, Equation (4) can also be numerically solved by using a novel method based on the conjugate-gradient algorithm. This treatment was first introduced by Duvillaret et al. in 1996.^[56] By using this approach, the complex refractive index is iteratively calculated from the measured THz response for most materials without any simplifications. Details of this numerical approach are in the original report.^[56]

2.4.2. Conductivity at THz Frequency Region

The complex conductivity of a material $\tilde{\sigma}(\omega) = \sigma_1(\omega) + i\sigma_2(\omega)$, which reflects the transport properties, can be derived from the complex refractive index by using both Maxwell's equation and Ohm's law^[62]

$$\tilde{n}^2(\omega) = 1 + \frac{4\pi i \tilde{\sigma}(\omega)}{\omega} \quad (7)$$

In addition to describing the transport properties, two key material parameters, charge carrier density and mobility, can be acquire from the frequency-resolved complex conductivity with the classical Drude model.^[43] In the case where the Drude model is applicable, the Drude response is written as

$$\tilde{\varepsilon}(\omega) = \frac{\sigma_{dc}}{1 - i\omega\tau} \quad (8)$$

where τ is a phenomenological relaxation time and the conductivity of the material within the Drude model is written as $\sigma_{dc} = Ne^2\tau/m$ with the charge density N , electronic charge e , and the effective mass of charge carrier m . Combining Equation (8) with the well-known Drude response, we get

$$\tilde{\varepsilon}(\omega) = \varepsilon_\infty - \frac{\omega_p^2}{\omega^2 + i\gamma\omega} \quad (9)$$

where ε_∞ denotes the high-frequency dielectric constant, γ is the damping rate, which corresponds to the scattering rate of carriers. The frequency of plasma oscillation ω_p is defined as $\omega_p^2 = Ne^2/\varepsilon_0 m$. The charge carrier concentration N along with the carrier mobility $\mu = e/m\gamma$ can be derived in the case where the effective mass m is known.

It should be pointed out that the charge concentration and carrier mobility can be determined only if the scattering times of charge carriers are in the scale of picoseconds, which correspond to a scattering rate at THz frequency. This leads to finite and dispersive values of frequency-resolved complex conductivity and dielectric response. In the case the scattering time is far beyond the picoseconds, only the pure imaginary dielectric response along with a finite real part of conductivity can be obtained.^[43] As a result, the carrier density and the scattering time cannot be independently determined. These properties enable the THz-TDS technique to be used as a powerful tool to study the effects of lattice vibration and defect scattering on the carrier relaxation

and transport properties in materials, where the lifetimes of such scattering are within the picoseconds time scale.

2.4.3. Lifetime of Photoexcited Carriers

In addition to extracting the frequency-resolved material properties, an optical pump–THz probe setup can also provide the possibility of monitoring the ultrafast dynamics process of photoexcited carriers in semiconducting 2D materials with both direct and indirect bandgaps. In optical pump–THz probe experiments, samples are photoexcited by the optical pulse and the dynamic processes of photoexcited charge carriers are then probed by THz pulse with time delay Δt . Since the time-resolved photoconductivity is measured using a time-dependent transient field $E(t)$, rather than a static field, the measured transmitted THz field is jointly dominated by the time t and the pump–probe time delay Δt . In pump–probe studies, it is more straightforward to present the measured physical quantities, such as transmission or conductivity, in terms of being frequency and time delay dependent, that is, $T(\omega, \Delta t)$ or $\tilde{\sigma}(\omega, \Delta t)$.

In addition to the optical pump–THz probe approach, the hot-carrier relaxation process can also be measured by using either ultrafast transient absorption (TA) or time-resolved photoluminescence (TRPL) techniques.^[66,67] Whereas TA and TRPL have the ability to measure the population dynamics of charge carriers, only the optical pump–THz probe measurement can provide the physical quantities in the frequency region. This is one of the major advantages of this approach compared with the other time-resolved charge concentration measurements. Figure 1d shows the measured photomodulated change in the transmission spectrum $\Delta T/T$ as a function of pump–probe delay time.

3. 2D vdW Materials

Since the discovery of single-layer graphene in the beginning of this century,^[1] much attention has been paid on the 2D vdW materials. To date, there are more than 500 types of materials that constitute the 2D vdW material family, which range from semimetallic graphene to semiconducting TMDs, and include main group metal chalcogenides (MMCs), transition metal trichalcogenides (TMTs), tetradymites, metal halides (MHs), transition metal chalcogenophosphates (TMCPs), phosphorene, silicene, germanene, and insulating h-BN.^[4,5,68,69] The spectral range of 2D vdW materials, which covers from the ultraviolet region for h-BN, to the visible region for TMDs and phosphorene, and to the radio frequencies for graphene, along with their corresponding crystal and electronic structures, is illustrated in Figure 2a–c.^[70] With the rapid development of chemical synthesis approaches, many novel 2D vdW materials have been successfully synthesized in recent years. However, till now most of the ultrafast THz spectroscopy studies were still focused on the conventional 2D-layered vdW materials such as graphene, h-BN, and TMD. In this section, we will focus our discussions on the synthesis approaches and the fundamental physical properties including the crystal geometry structures,

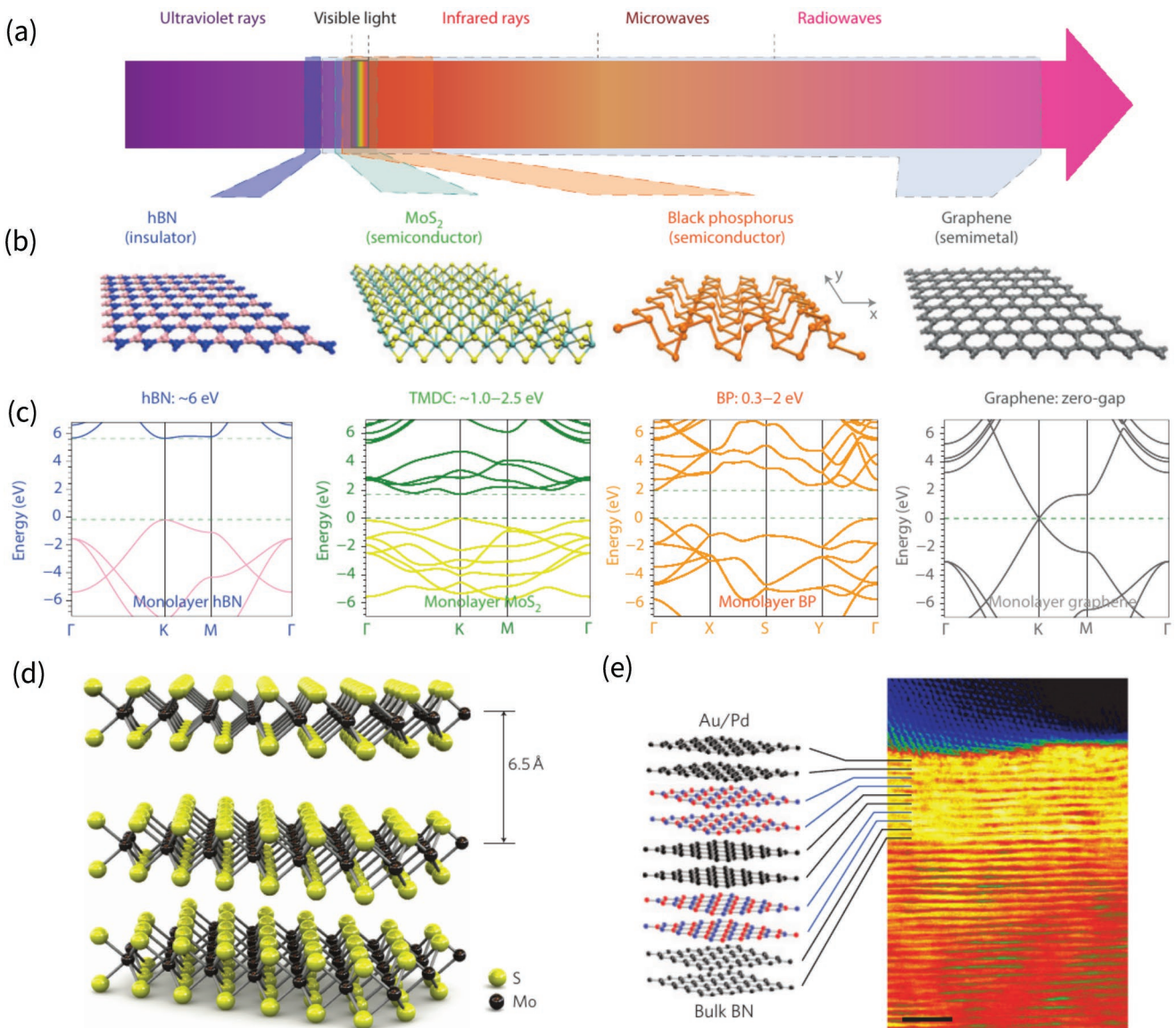


Figure 2. a) Broad spectral range of 2D vdW materials covering from ultraviolet rays to radiowaves with b) the corresponding crystal structures and c) electronic band structures of insulating h-BN, semiconducting TMDs, black phosphorus, and semimetal graphene. a–c) Reproduced with permission.^[70] Copyright 2014, Springer Nature. d) 3D representation of the crystal structure of layered MoS₂. Reproduced with permission.^[71] Copyright 2011, Springer Nature. e) Image of bright-field cross-sectional STEM of a stack of graphene and h-BN bilayers. Reproduced with permission.^[72] Copyright 2012, Springer Nature.

the electronic band structures, and the characteristics of the optical absorption and emission processes of graphene and conventional inorganic semiconductor 2D vdW materials, especially for TMDs and phosphorene.

3.1. Crystal Structure

The crystal structures of layered 2D vdW materials are commonly constructed by neutral single-atom-thick layers, such as graphene and h-BN, or by neutral polyhedral-thick layers, such as black phosphorus and TMDs. The geometry of h-BN, MoS₂, black phosphorus, and graphene with single-layer 2D crystal structures is presented in Figure 2b. Compared with the

covalent or ionic connections between atoms within each layer, these neutral single-atom- or polyhedral-thick layers are stacked together via vdW interaction in the z-direction to form layered crystals. The crystal structure of multilayer MoS₂, which is composed of vertical stacks, is illustrated in Figure 2d. Figure 2e presents the bright-field cross-sectional scanning transmission electron microscopy (STEM) image of a stacked graphene and h-BN bilayer structure.^[72] The STEM imaging reveals the clear atomic layer structures of vdW-stacked materials.

3.2. Synthesis

Growth of single- or few-layer (also named as mono- or multi-layer) 2D vdW materials is the starting point to investigate

their physical properties and to develop 2D electronic and optoelectronic devices. The most commonly used approach to fabricate single- or few-layer 2D vdW materials is mechanical or chemical exfoliation.^[4] The idea of the exfoliation method comes from the characters of layered vdW materials, in which atoms are strongly and covalently bonded together with their neighbors in the same layer, and the different layers are weakly held together by vdW interactions with energies of tens of milli-electron volts. These properties enable the exfoliation of layered materials possible.

Mechanical exfoliation has a long history for preparing few-layered vdW materials since the 1960s.^[73] To date, this approach remains as one of the most powerful methods to fabricate high-quality single- or few-layered 2D materials with large sizes on different substrates. Moreover, compared with the other synthesis approaches, the atomic layers of vdW materials are considerably less destructive during mechanical exfoliation. In addition to the “Scotch tape” exfoliation, another way to exfoliate layered 2D vdW materials is chemical exfoliation. The working principle of chemical exfoliation is to break the vdW interactions between different layers via the surface tension of solvent. By immersing into a polar solvent, the atom layers of a vdW material are exfoliated by the surface tension and then dispersed into the solvent. To date, the single- or few-layered crystal structures of many novel vdW materials, such as CaGe₂, GeH, and Ti₃C₂ (OH)₂, have been successfully exfoliated by using the chemical exfoliation approach.^[4,74,75]

In addition to the chemical and mechanical exfoliation, large-area chemical vapor deposition (CVD) is another important approach to synthesize large size, high-quality single-layer vdW materials, especially for graphene.^[76,77] In contrast to the exfoliation approaches, thin graphene layers are grown on the substrate with the deposition of a small carbon–hydrogen molecule, like methane, instead of exfoliation from bulk graphite. Successful synthesis of single-layer graphene was first achieved by growing graphene layer on copper foil via the low-pressure CVD approach.^[77] Later, single- or few-layer graphene with high homogeneity and a domain size of several hundred micrometers to even millimeters were reported.^[78] This enables a further study on the mechanisms of photoconductivity of single-layer graphene. In contrast to graphene, to synthesize other vdW materials composed of two or more elements through CVD is much more complicated. Further progress on the CVD synthesis of 2D vdW materials, for example, h-BN and MoS₂, has been reported elsewhere.^[4,79]

Although the large-area CVD provides the possibility of synthesizing large-size graphene layers with single- or few-layered crystal structures, the complex synthesis process limits its applications in compound vdW materials. A much more appealing and versatile synthetic strategy is the vapor deposition approach, which has widely been used to fabricate low-dimensional nanostructures, for example nanowires, nanotubes, and thin films. The vdW epitaxy approach can generate 2D flakes composed by either the same or different material(s). This enables the fabrication of a crystalline 2D vdW heterostructure. Details of the synthesis of 2D vdW heterostructures using vapor deposition approach can be found in elsewhere.^[4]

Another important chemical approach to synthesize 2D vdW materials is the solution-phase growth method. As an

important solution-phase approach, the colloidal growth reaction offers a fast and low-cost way to produce 2D materials at the gram scale quantity with high quality.^[80,81] Compared with exfoliation and large-area CVD methods, the in-plane sizes of 2D materials synthesized using solution-phase growth approach are around tens to hundreds of nanometers with thicknesses from a single layer to tens of nanometers. To date, an accurate control of the thickness and the lateral dimensions of 2D vdW materials during the reaction of solution-phase growth have yet to be established. Recently, some breakthroughs on the synthesis of 2D graphene nanosheets, graphene quantum dots, and phosphorene nanosheets with high quality have been reported.

3.3. Electronic Properties

3.3.1. Energy Band Structures

The electronic band structure dominates the electronic and optical properties of a material. Good knowledge of electronic structures is the essential first step to understand the fundamental physics of 2D vdW materials and to design the corresponding electronic and optoelectronic devices. To actually measure the electronic band structures of 2D vdW materials remains a difficult task in experiment. A state-of-the-art powerful experimental approach probe of the band structures of the occupied states is angle-resolved photoemission spectroscopy (ARPES).^[39,82] In addition to ARPES, the band structures of the unoccupied state and the charge transfer process of 2D vdW materials can be measured using inverse photoelectron spectroscopy.^[83]

In contrast to these delicate experiments, ab initio calculations provide an alternative path to obtain the electronic band structures of 2D vdW materials. Within the framework of ab initio calculations, DFT is one of the most powerful tools for studying the electronic band structures of materials with various sizes and dimensions. By approximating the complex many-particle interactions as a response of charge density, DFT maintains a sufficient accuracy for the band structure calculation, especially for the dispersion relations, with an acceptable computational cost.^[62,84] The success of DFT is based on attaining a single-particle Schrödinger equation to study the electronic structures of many-particle systems at the ground state by treating the many-body effects as a function of charge densities. Band structures obtained from DFT calculations have excellent quality, especially for the dispersion relations. The DFT-calculated dispersion relation of the electronic structures of single-layer graphene is presented in Figure 3a. As shown in this figure, linear energy dispersion curves are located around the K point in the Brillouin zone (BZ) with the crossing point referred to as the Dirac point. In an undoped graphene without photoexcitation and charge carrier injection, the Fermi level crosses the Dirac point. Moreover, around the Dirac point, the energy dispersion is linear with electrons behaving as massless relativistic particles. This leads to graphene being an unusual gapless semimetallic material with novel electronic and optical characteristics. The detailed electronic properties of graphene can be seen in a previous review.^[85]

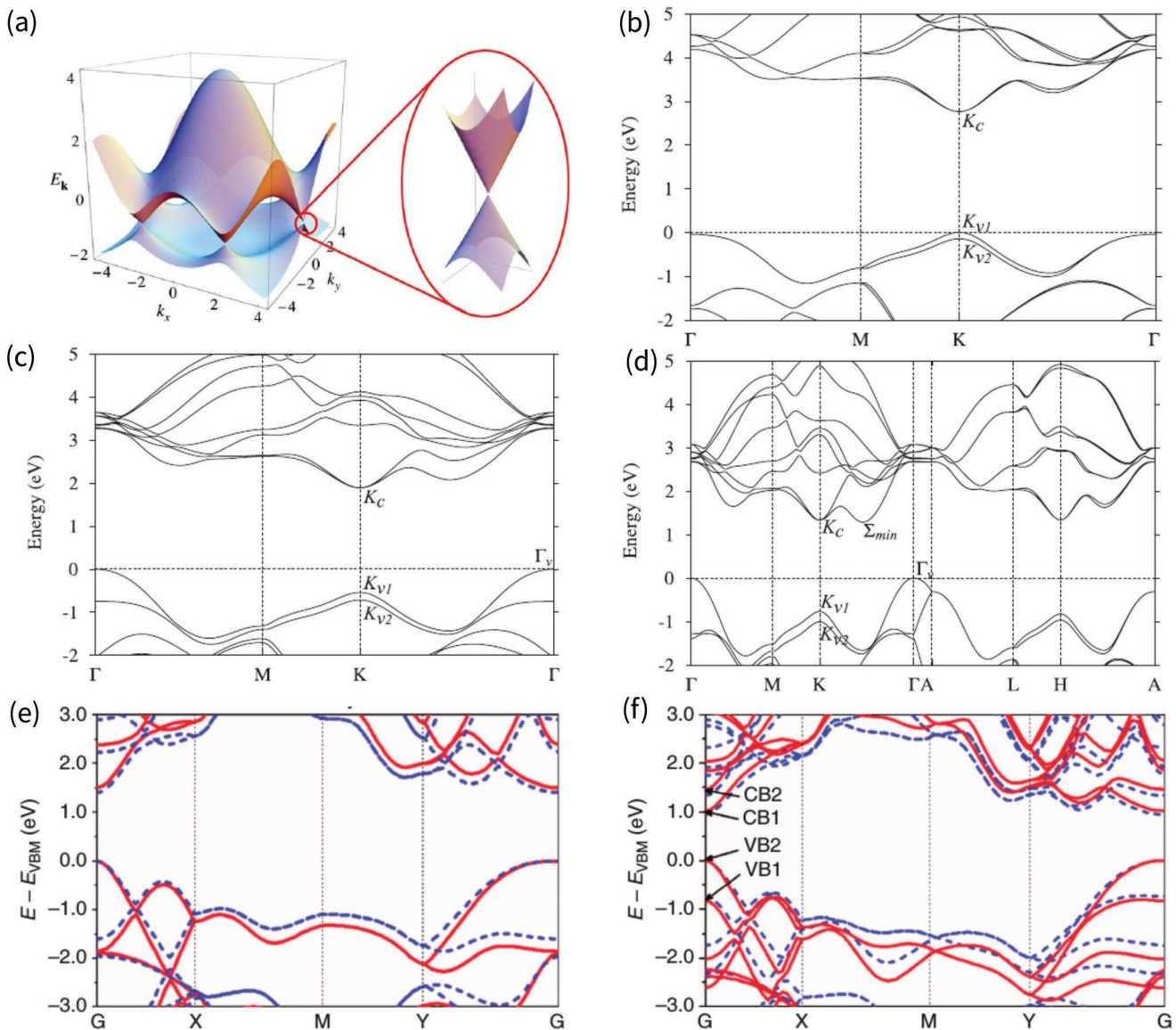


Figure 3. a) Electronic dispersion in the honeycomb lattice of graphene, with a zoom-in of the energy bands close to one of the Dirac points. Reproduced with permission.^[85] Copyright 2009, American Physical Society. Calculated band structures of b) single-layer, c) double-layer, and d) bulk MoS₂ using the quasiparticle self-consistent GW method. b-d) Reproduced with permission.^[86] Copyright 2012, American Physical Society. Band structures of e) single-layer and f) double-layer phosphorene obtained from DFT calculation using the HSE06 exchange-correlation functional (red solid line) and the local density approximation-modified Becke-Johnson (LDA-mBJ) potential (blue dashed lines). e,f) Reproduced with permission.^[88] Copyright 1965, Nature Publishing Group.

3.3.2. Bandgaps and Spin Splitting

Although DFT-based calculations have provided successful descriptions of the gaplessness graphene band structures and the dispersion relations of semiconducting 2D vdW materials, the peculiarity of the density functional approach limits its further applications to calculate the energy difference between the highest valence band and the lowest conduction band of the semiconducting or insulating 2D vdW materials. Owing to the limitation of the charge density functional frame, the charge densities of the unoccupied Kohn-Sham orbits are meaningless in physics. As a consequence, the bandgaps between the occupied and unoccupied states obtained from

DFT calculations are underestimated. Moreover, due to the reduction of the dielectric screening, 2D vdW materials exhibit a strong electron correlations effect, which weakens the validity of the DFT approach.

A more rigorous band structure calculation is possible using the GW approximation to treat the self-energy corrections from many-electron interactions.^[88] Within this approach, the self-energy correction Σ is truncated at the first-order expansion as $\Sigma = iG\Gamma$, where G denotes the single particle Green function and Γ is the screened Coulomb interaction. Band structures of layered and bulk MoS₂ calculated by using a quasiparticle self-consistent GW approximation are presented in Figure 3b-d, respectively.^[86] In contrast to the gapless graphene, energy gaps

between 1 and 3 eV are obtained in the bulk and layered MoS₂ from GW calculations.

As indicated in Figure 3b–d, the characteristic of MoS₂ changes from an indirect bandgap semiconductor in the form of bulk or few-layer structures to a direct bandgap material in the form of single-layer structure. This transition is the result of the reduced interlayer coupling, which shifts the minimum value of the conduction band to the K point of the BZ, which is the position of the valence band maximum (VBM) in reciprocal space. In addition, a large energy splitting of around hundreds of meV, appears at the VBM at the K point of the BZ in both layered and bulk MoS₂. This valence band splitting is the result of the strong spin–orbit coupling along with an interlayer interaction in 2D vdW transition-metal compounds. Beyond MoS₂, other layered TMD materials, for example, MoSe₂, WS₂, and WSe₂, exhibit similar electronic band structures, including the indirect-to-direct band structure changing by reducing the thickness of material to single-layer structure, and the large valence band splitting at the K point of the BZ.

In contrast to layered TMD materials with thickness-dependent indirect-to-direct band transition, black phosphorus is a direct bandgap material with the values of bandgap being increased from 0.3 to 1.88 eV when the thickness of the material decreases from the bulk structure to single-layer structure (also named as phosphorene). The calculated band structures of single- and double-layer phosphorene using DFT with the Heyd–Scuseria–Ernzerhof (HSE) framework of an exchange-correlation functional^[89] are presented in Figure 3e,f, respectively.^[87] We can see that both single-layer and few-layer black phosphorus are a novel category of 2D semiconductors offering direct bandgaps. Moreover, owing to the weak spin–orbit coupling strength in phosphorus, the spin splitting in the valence band of few-layered black phosphorus and phosphorene can be simply neglected.

3.3.3. Valleytronics

In a direct bandgap material, the minimum (maximum) value of the conduction (valence) bands is normally located at high symmetry points in the BZ, which are K and –K points for 2D vdW materials with a hexagonal crystal structure. These band minima (maxima) are commonly referred to as valleys. In 2D materials with a break of inversion symmetry, for example, single-layer TMDs or double-layer graphene under bias, electrons, and holes located at the energy valleys with opposite momentums “feel” the interaction from effective magnetic fields with opposite directions. These effective magnetic fields are induced by the corresponding Berry curvatures. This leads to the so-called “valley” degrees of freedom.^[90,91] Moreover, the orbital angular momentum of charge carriers also makes contributions on the valley magnetic moment. In 2D vdW materials with large spin splitting, the opposite spin signs of the spin splitting exhibit opposite momentums in reciprocal space as a result of the time-reversal symmetry. The strong spin–valley coupling leads to interesting consequences, such as increasing the lifetime of spin and valley polarization, a manipulation of the spin polarization by using the valley properties, and introduction of new selection rules for the excitation of

carriers with certain spin sign to a valley with certain sign of momentum.^[4,92] The valley-dependent electronic structures of TMD along with the optical selection rules for the spin-valley coupling system are presented in Figure 4.^[92,93]

3.4. Optical Properties

The optical property of a material is a wide topic, as it defines how the material interacts with light, which includes refraction, absorption, emission, photoluminescence, diffraction, photovoltaic, and photocatalytic. In this section, we will focus on the absorption and emission (i.e., photoluminescence in experiments) properties of 2D vdW materials, which are related to the physical quantities obtained from THz-TDS and optical pump–THz probe measurements. In physics, the absorption and PL properties of a material are determined by its electronic band structures and exciton (bound electron–hole pair) states. As a consequence of the valence band splitting, two direct bandgap transitions are available in TMDs with single-layer structure. Two exciton emission peaks, which are commonly referred to as A- and B-peaks, are observed in the PL spectra of 2D TMDs. A-peak corresponds to a narrow bandgap energy transition with strong emission intensity, whereas the bandgap energy transition of B-peak is larger and the emission intensity is weaker. As the opposite process, these two peaks also exist in absorption spectrum. The absorption and emission of both the A and B excitons have been measured using absorption and PL spectroscopy techniques in experiment and calculated by using the Bethe–Salpeter equation (BSE)^[94] based on the GW-calculated quasiparticle band structures in theory.

Figure 5a,b shows the measured PL and absorption spectra of layered MoS₂, respectively. Compared with the PL spectra of monolayer MoS₂, the PL spectrum intensities of MoS₂ with 4–6 layers are enlarged in Figure 5a. Besides the significantly changed spectrum intensity, the PL spectral shapes of single- and few-layer MoS₂ are also quite different from each other. A single narrow peak centered at around 1.9 eV with a 0.05 eV spectrum width appears in the PL spectrum of single-layer MoS₂. In contrast to the simple spectral shape of monolayer MoS₂, multiple emission peaks (peaks A, B, and I) appear in the PL spectra of few-layer MoS₂. Peaks of A, B, and I exciton emission or absorption are labeled in Figure 5a,b.^[34] For the measured spectral shape, peaks A and B are attributed to two absorption resonances of direct-gap hot luminescence, whereas peak I is the result of indirect-gap luminescence. Theoretically calculated A- and B-exciton absorption peaks using the GW+BSE approach along with the corresponding experiments are given in Figure 5c–f.^[27]

4. Time-Resolved Optical Process of 2D vdW Materials

Although many time-resolved spectroscopy techniques, such as ultrafast transient absorption spectroscopy and time-resolved PL spectroscopy, have the ability to track the dynamic population statistics of the total electron–hole pairs, only THz-TDS-based measurements can provide the frequency-resolved

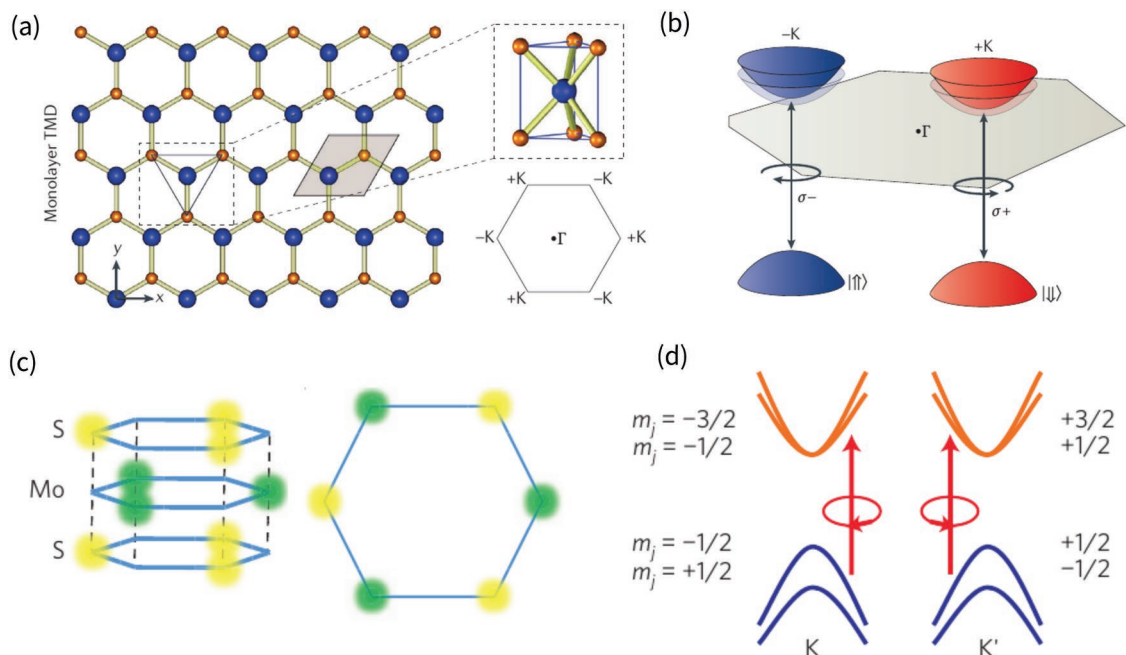


Figure 4. a) 2D hexagonal crystal structure of monolayer TMD composed of transition metal atoms (blue) and chalcogen atoms (orange) resembling that of graphene but with broken inversion symmetry. A side view shows its corresponding 3D structure (upper part), and the BZ with labeling of the Γ point and the two inequivalent $+K$ and $-K$ points (lower part). b) Valley-dependent optical selection rules for interband transitions in monolayer TMDs. σ^+ polarized light couples to the $+K$ valley, and σ^- polarized light couples to the $-K$ (blue) valley. a,b) Reproduced with permission.^[93] Copyright 2013, Springer Nature. c) Representation of the trigonal prismatic structure of monolayer MoS₂ with its honeycomb lattice structure. d) The lowest-energy conduction bands and the highest-energy valence bands labeled by the z-component of the total angular momentum near the K and K' points in the BZ, along with their corresponding selection rules. c,d) Reproduced with permission.^[94] Copyright 1951, Nature Publishing Group.

complex photoconductivity within a femtosecond time scale. As a consequence, optical pump–THz probe spectroscopy provides an opportunity to monitor the ultrafast dynamic processes of photoexcited charge carriers, excitons, trions, and biexcitons with the changes of photoconductivity. Moreover, as the exciton-binding energies of 2D materials are covered in the energy range of THz radiation, THz probes can sensitively discriminate the free charge carriers and excitons. The properties of THz-TDS enable it as a powerful tool to investigate the ultrafast dynamics of photoexcited quasiparticles and the optical properties of 2D materials.

4.1. Excitons, Trions, and Biexcitons

Following a nonresonant photoexcitation on a semiconductor, the photoexcited electrons and holes attract by each other through a Coulomb interaction. Attraction between charge carriers causes their motion to be correlated and the resultant electron–hole pair is known as an exciton.^[95] The reduced dielectric screening and strong quantum confinement in 2D vdW materials lead to the strong Coulomb interaction in these materials. The formations of bound excitons from unbound electron and hole pairs in 3D bulk material and in monolayer 2D material are schematically illustrated in Figure 6a. Based on the sizes of bound electron–hole pairs, excitons are commonly divided into Wannier–Mott and Frenkel excitons in conventional semiconductors. In the case of Frenkel excitons, electron–hole pairs are strongly coupled and are localized in one or two unit cell(s).

The Wannier–Mott exciton, which is characterized by a weak Coulomb interaction, corresponds to a large exciton size with the electron and hole moving in a homogeneous dielectric background. Excitons with both Frenkel and Wannier–Mott characteristics and large binding energies in 2D vdW materials dominate the optical properties, and lead to the different properties of 2D vdW materials compared with conventional semiconductors. For single-layer MoS₂, theoretical calculations show excitons with a binding energy of 0.63–1.04 eV and a radius of around 1.0 nm.^[27,96] Exciton wavefunctions of single-layer MoS₂ obtained from ab initio calculations are presented in Figure 6b. Because the novel physics in 2D vdW materials, such as the spin–valley interaction and defect-induced optical processes, is closely related to the strongly bound excitons, the exciton state is the subject of intense investigations.^[97,98]

As well as the electrically neutral excitons, additional free electrons and holes obtained from the substrate, vacancies, and adsorbates of 2D vdW materials lead to the formation of more localized excitations, which consist of three charged particles. This type of charged quasiparticle is known as a trion. Trions, with binding energies of around 20 meV, have been observed in monolayer MoS₂ by means of absorption and PL spectroscopy. The large binding energy of a trion in 2D vdW materials results from both the strong quantum confinement and dielectric screening effects. The large trion binding energy plays the significant role on the novel physical properties of 2D vdW materials even at room temperature, which are missing in conventional semiconductors.^[93] In addition to trions, two neutral excitons or an exciton with a charged trion can bind

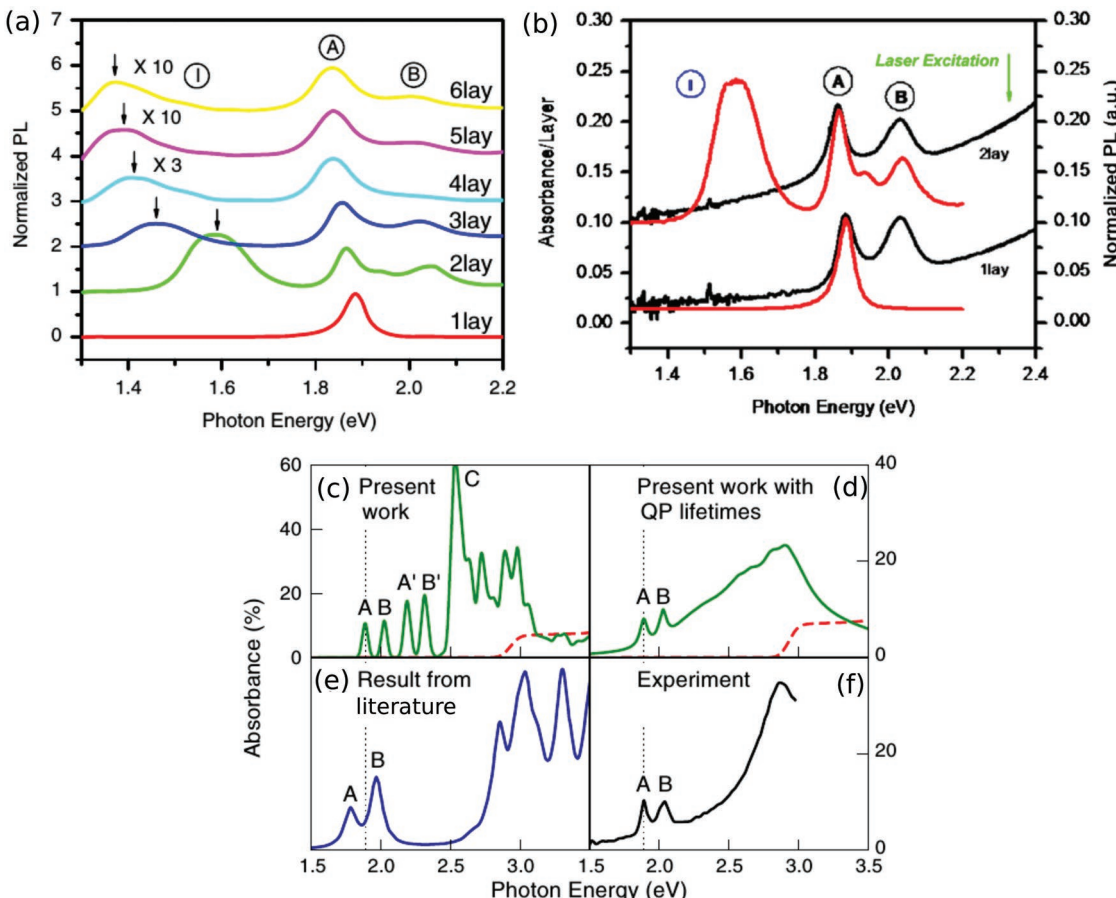


Figure 5. a) Normalized PL spectra by the intensity of peak A of thin layers of MoS₂ with layer numbers from 1 to 6. Feature I for $N = 4\text{--}6$ is magnified as three times for the case of 4 layered structure and ten times for 5 and 6 layered structures and the spectra are displaced for clarity. b) Absorption spectra (left axis, normalized by N) and the corresponding PL spectra (right axis, normalized by the intensity of the peak A). The spectra are displaced along the vertical axis for clarity. a,b) Reproduced with permission.^[96] Copyright 2013, American Physical Society. c) Absorption spectra of MoS₂ without (dashed red curve) and with (solid green curve) electron–hole interactions plotted with a constant broadening of 20 meV. d) The same calculated data as in panel (c) but using an ab initio calculated broadening based on the electron–phonon interactions. e) Non-self-consistently calculated G₀W₀ absorption spectrum. f) Measured absorbance from experiments. c–f) Reproduced with permission.^[97] Copyright 2018, American Physical Society.

with each other to form a neutral or charged biexciton through a strong Coulomb interaction in 2D materials with dielectric screening.^[101] An illustration of an exciton (X), trion (T), neutral biexciton (XX), and charged biexciton (XT) in single-layer MoSe₂ is given in Figure 6c.^[100,101] The formation rates of excitons, trions, and biexcitons are functions of the excitation power. As was shown previously,^[100] the populations of excitons, trions, and biexcitons in double-layer WS₂ increase with increasing the excitation laser power intensity with slopes of 0.9, 1.2, and 1.6, respectively.^[100] This property is induced by the increase of free charge carrier density with increasing excitation photon numbers.

4.2. Formation of Exciton State

In most of the experiments with photoexcitations, electrons and holes are typically excited through nonresonant optical excitations with energies higher than the exciton resonance. The high-energy charge carriers are expected to relax toward the

conduction band minimum (CBM) and the VBM, and then form excitons through a Coulomb interaction. A mixture of bound and unbound quasiparticles exists during this process. An observation on the evolution of these quasiparticles of 2D vdW materials after photoexcitation is of central importance to study the ultrafast dynamics of excitons in such systems. Owing to the similar response of bound and unbound charge carriers in optical interband spectroscopy, direct observation of the exciton formation process is a challenging task for optical spectroscopy studies.

To investigate the physics involved in the exciton formation process in 2D vdW materials, Steinleitner et al. performed a resonant/nonresonant optical pump field-sensitive THz femtosecond probe measurement in 2017 and reported the ultrafast exciton formation process in single-layer WSe₂.^[42] The working principle of their measurement is given in Figure 7a. As shown in this figure, excitons absorb radiation efficiently with energy of the intraexcitonic resonances, which correspond to the transitions between the ground and the excited states. In contrast to the bound excitons, the unbound charge carriers are transferred under the driving of the THz field instead of absorbing

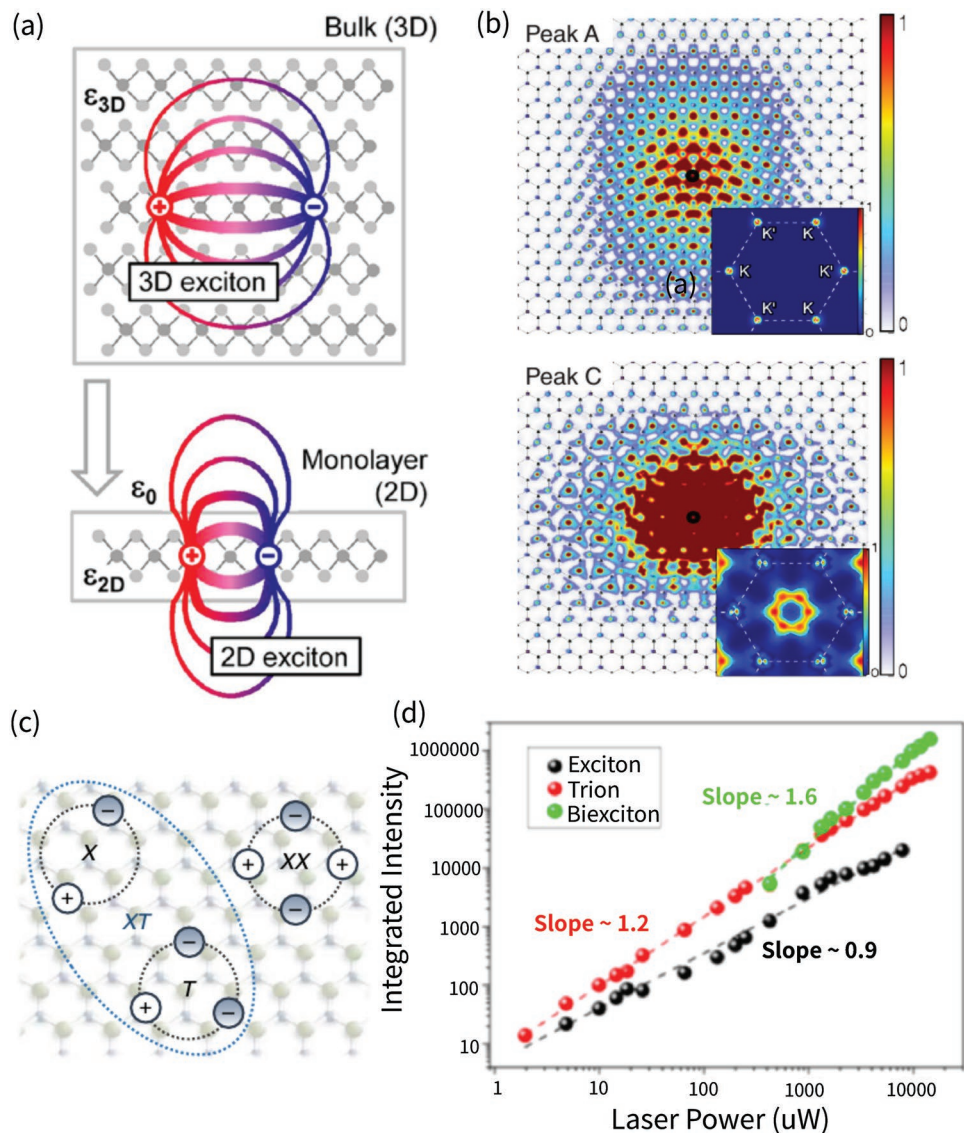


Figure 6. a) Real-space representation of electron and hole bound into an exciton for the 3D bulk and a quasi-2D monolayer. The changes in the dielectric environment are indicated schematically by different dielectric constants ϵ_{3D} and ϵ_{2D} and by the vacuum permittivity ϵ_0 . Reproduced with permission.^[99] Copyright 2014, American Physical Society. b) The modulus squared of MoS₂ exciton wavefunction projected onto the plane with the hole (black circle) fixed near a Mo atom in real space for two exciton peaks (peaks A and C). Reproduced with permission.^[27] Copyright 2013, American Physical Society. c) Real-space representation of the formation of charged XT and neutral XX biexcitons. d) Logarithmic plot of the PL integrated intensity of the exciton, trion, and biexciton peaks versus laser excitation power. c,d) Reproduced with permission.^[103] Copyright 2018, American Chemical Society.

radiation. By monitoring the change of the complex conductivities after photoexcitation, the evolution of the excitons and unbound electron–hole pair population is obtained. In their experiment, the samples were optically excited by highly nonresonant (3.04 eV) and resonant (1.67 eV) femtosecond photoexcitation, respectively. The probe light was a mid-infrared (mid-IR) pulse with a spectrum covering frequencies between 30 and 53 THz. The pump-induced THz response changes $\Delta\sigma_1$ (real part of photoconductivity) and $\Delta\epsilon_1$ (real part of dielectric response) with resonant and nonresonant excitation are shown in Figure 7b. As presented in Figure 7b, the phase shift comparing to the reference of exactly π in the left column (resonant excitation) shows the hallmark of an absorptive response,

whereas the relative phase shift that deviates strongly from π in the right column (nonresonant excitation) indicates the response of a plasma.^[42] The ultrafast evolution of THz probes for a nonresonant excited electron–hole system with different pump–probe time delay is given in Figure 7c. As shown in this figure, an electron–hole plasma-like response appears in the real parts of the measured complex photoconductivities and dielectric functions at a time delay of $t_{pp} = 0$ fs. After 0.4 ps of photoexcitation, the observed increase of signal intensity with spectrum broadening corresponds to the 1s–2p absorption process monitored with resonant excitation. The result indicates an increase of the exciton populations. For t_{pp} longer than 0.8 ps, both values of $\Delta\sigma_1$ and $\Delta\epsilon_1$ decrease, which corresponds to the

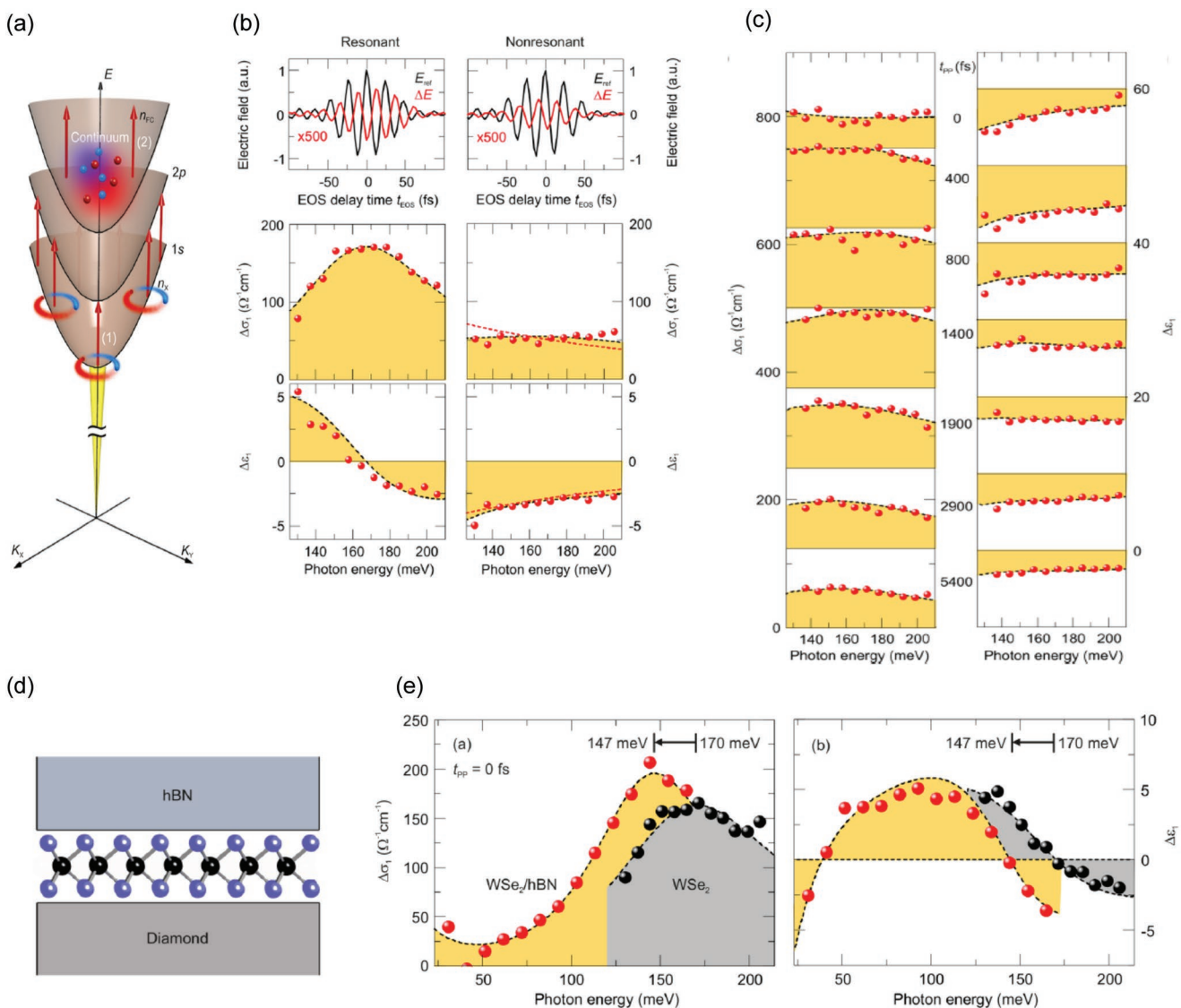


Figure 7. a) Schematic illustration of the low-energy response of excitons and unbound electron–hole pairs. The dispersion relations of exciton states with the principal quantum numbers $n = 1, 2, 3$, and the electron–hole continuum (topmost band). b) Upper: time-resolved waveforms of the probe pulse transmitted through the sample without excitation (black curve) and the pump-induced change ΔE (red curve). Bottom: corresponding pump-induced changes of the real part of the optical conductivity and the dielectric function as a function of the photon energy. Red circles and black-dashed lines correspond to the experimental data and the results from the Drude–Lorentz model, respectively. The left and right columns correspond to the resonant and nonresonant excitations, respectively. c) Pump-induced changes of the real parts of the complex optical conductivity (left column) and the dielectric function (right column) of the photoexcited WSe₂ monolayer as a function of the photon energy for several pump delays t_{pp} after nonresonant excitation. a–c) Reproduced with permission.^[42] Copyright 2017, American Chemical Society. d) Schematic illustration of the WSe₂/h-BN heterostructure on a CVD diamond substrate. e) Pump-induced changes of the real parts of the optical conductivity and the dielectric function as a function of the photon energy. d,e) Reproduced with permission.^[106] Copyright 2005, American Chemical Society.

carrier recombination process. This THz-TDS based measurement provides an opportunity to observe the ultrafast exciton formation process directly. Based on these measurements, more than half of the photoexcited charge carriers are bound to form excitons within few sub-picoseconds.

Shortly after measuring the exciton formation process in bare single-layer WSe₂, Steinleitner et al. extended their studies to WSe₂/h-BN 2D heterostructures.^[103] A schematic illustration of the heterostructure studied in ref. [103] is given in Figure 7d. This heterostructure offers a unique ability to tailor dielectric

screening in 2D vdW materials and to fundamentally change the formation process of excitons. A comparison between the THz response, including the values of $\Delta\sigma_1$ and $\Delta\epsilon_1$ of the WSe₂/h-BN heterostructure and of a single-layer WSe₂ is shown in Figure 7e. In the case of uncovered single-layer WSe₂, a peak value of $\Delta\sigma_1$ with a zero crossing of $\Delta\epsilon_1$ was obtained with the photoenergy as high as 0.17 eV. The observations correspond to a resonant absorption of the 1s–2p exciton transition. Compared with the bare single-layer WSe₂, the characteristic peak in $\Delta\epsilon_1$ of the WSe₂/h-BN heterostructure was obtained with an

photoenergy of 0.147 eV and had a narrower resonance. These characteristics are the results of renormalized 1s–2p transition under a resonant photoexcitation in the 2D WSe₂/h-BN heterostructure with custom-tailored dielectric screening and electronic correlations.

In addition to the measurements on the exciton formation processes of bare and covered single-layer WSe₂,^[42,103] the concept of optical pump–broad band THz probe spectroscopy has also been employed to explore the exciton formation processes in other 2D vdW materials.^[102,104,105]

4.3. Recombination of Excited Charge Carriers and Excitons

4.3.1. Carrier Dynamics in Graphene

Optical pump–THz probe spectroscopy studies on the ultrafast dynamics of photoexcited charge carriers in graphene or graphite film have been conducted shortly after the discovery

of single-layer graphene. A pioneering THz spectroscopy work on graphite films was first performed in 2005 to study the photoexcited THz response of a graphite film with a thickness of 17 nm.^[106] The photoinduced frequency-resolved dielectric function changes were extracted from the measured THz transmission spectrum. The extracted imaginary part of the dielectric function was found to increase with a frequency below 15 THz and decrease with a frequency above 15 THz after photoexcitation. This character was explained as the results of competition between the direct and indirect optical transition processes in graphite films induced by the photoexcited hot electrons.

Different to the previous studies which were mainly focused on graphite films,^[106] George et al. reported the photoexcited charge carrier dynamics in epitaxial graphene with thicknesses of 12 and 20 atom layers using optical pump–THz probe spectroscopy.^[107] In their experiments, samples were photoexcited by an ultrafast laser of 760 nm wavelength and the probe THz pulses with bandwidth between 0.3 and 3.0 THz. Figure 8a

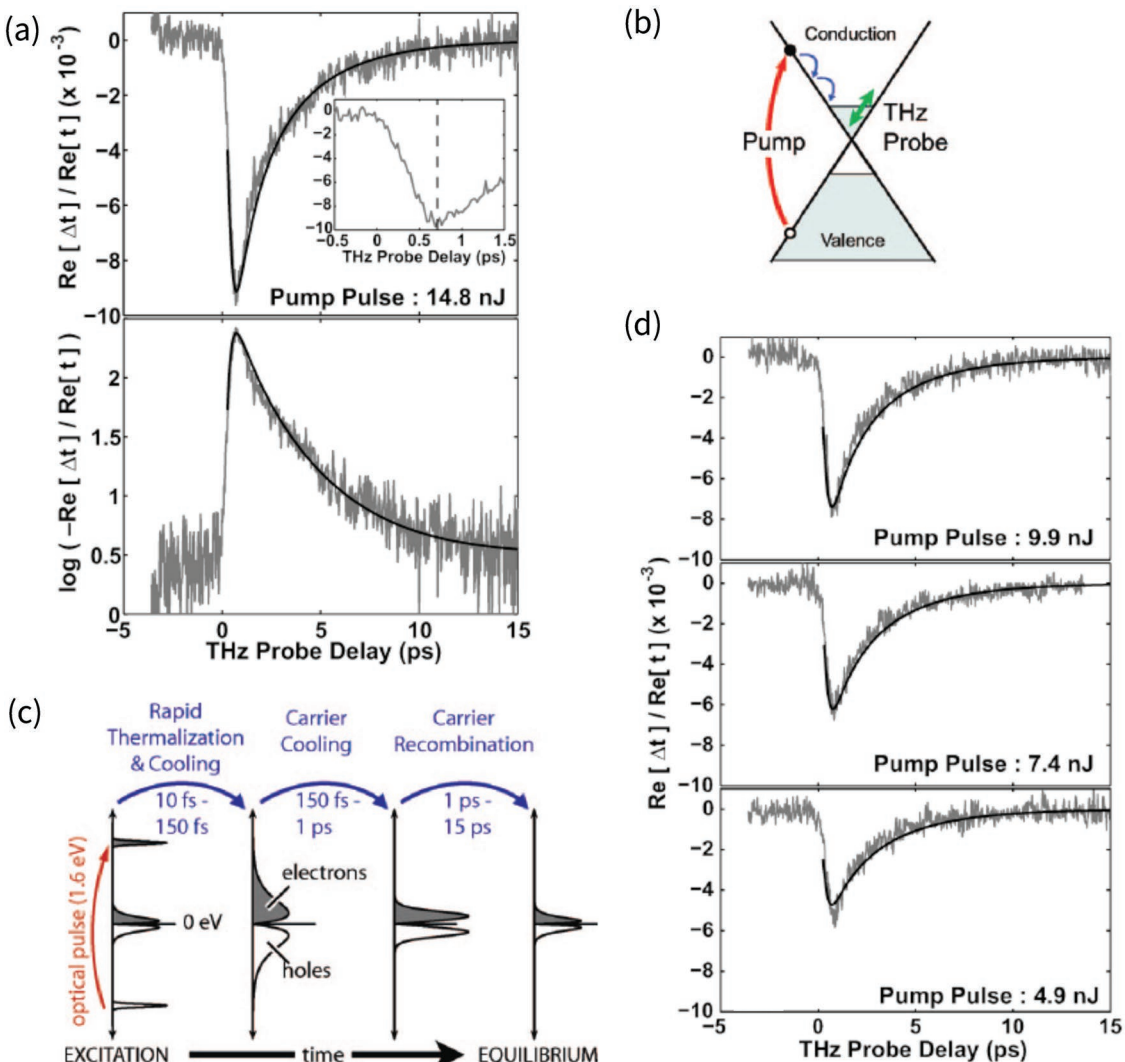


Figure 8. a) Upper: Measured change in the real part of the complex THz transmission (gray) with fitting curves (black). Bottom: The same data plotted on a logarithmic scale. b,c) A schematic of the rapid and the slow dynamic processes. d) Real part of the THz transmission with optical pump fluences of 9.9, 7.4, and 4.9 nJ. a-d) Reproduced with permission.^[110] Copyright 2015, American Chemical Society.

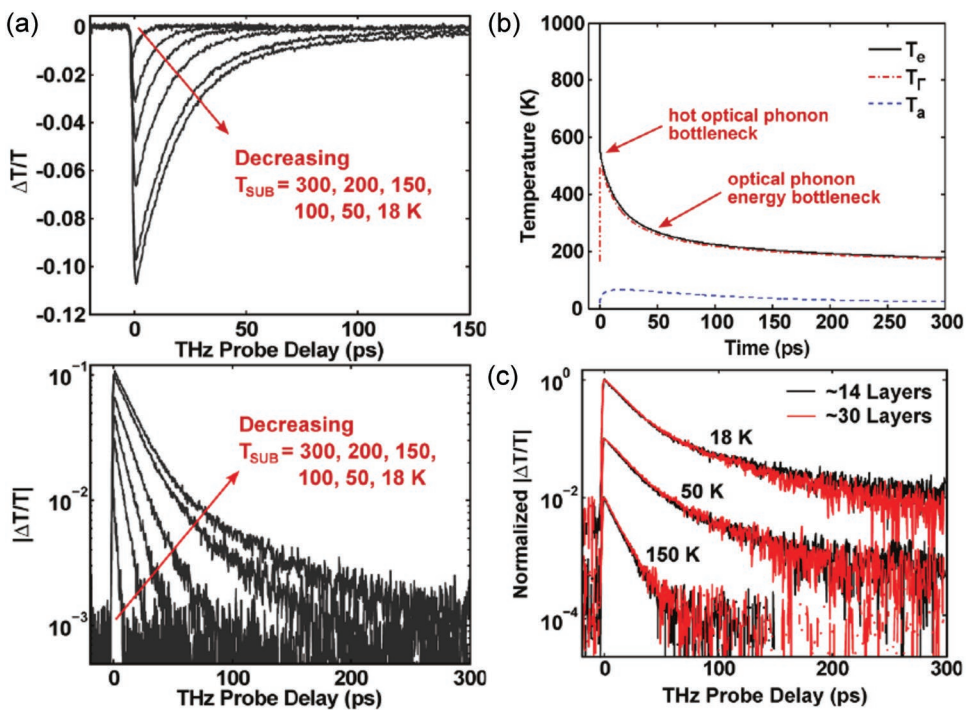


Figure 9. a) Upper: Measured time-resolved THz transmission $\Delta T/T$ as a function of time delay at substrate temperatures $T_{\text{sub}} = 300, 200, 150, 100, 50$, and 18 K . Bottom: The same data plotted on a logarithmic scale. b) Simulated electronic temperature T_e , optical phonon temperature T_Γ , and acoustic temperature T_a as a function of time delay after photoexcitation. c) Measured $\Delta T/T$ transients for samples with thicknesses of 14 atom layers (black line) and 30 atom layers (red line). a–c) Reproduced with permission.^[111] Copyright 2014, American Chemical Society.

shows the measured changes of the real part THz transmission for the thin sample (12 atom layer thickness) excited by an optical pulse with an energy of 14.8 nJ. The dynamic processes can be separated into two parts, that is, a rapid decreasing process with a time of around 1 ps (vertical dashed line in the insert) and a slow increasing process starting from 1 to 15 ps. These two relaxation processes are schematically illustrated in Figure 8b,c. Immediately following the photoexcitation, the nonresonantly excited electrons and holes are nonthermally distributed from the band edge. A hot Fermi-Dirac distribution is subsequently formed within 10–150 fs. Following this rapid thermalization, the hot charge carriers are cooled down to the band edge within 150 fs and 1 ps through intraband phonon scattering. After cooling down the hot carriers to the band edge, the nonradiative electron-hole recombination process dominates the photoconductivity and the THz transmission within time between 1 and 15 ps. Figure 8d shows the ultrafast carrier dynamic processes under different pump power densities. As indicated in this figure, the recombination time decreases by increasing the energy density of pump light. Moreover, the Auger process was identified to dominate the nonradiative recombination process. However, other recombination channels, such as plasmon and phonon emission processes, cannot also be simply neglected.

To further understand the cooling process of hot electrons in graphene excited by laser pulse, Strait et al. performed optical pump–THz probe spectroscopy measurements on graphene samples with various substrate temperature.^[108] In their experiments, graphene samples with a thickness of 14 atom layers were

grown epitaxially by thermal decomposition on substrates.^[109] Optical pump excitations were performed using ultrafast laser with 780 nm wavelength and a maximum energy of 114 nJ. The ultrafast nonequilibrium carrier dynamics in graphene samples were obtained via monitoring the time-resolved THz response. The measured time-resolved THz transmissions of samples with the substrate temperature from 18 to 300 K are presented in Figure 9a. The recovery time of THz transmission increases with an order of magnitude when the substrate temperature decreases from 300 to 18 K. To understand the temperature-dependent carrier relaxation process, Strait et al. simulated the electronic temperature, and the phonon temperature of both optical and acoustic modes with different time delays. Simulation results with $T_{\text{sub}} = 18 \text{ K}$ are given in Figure 9b. In this figure, the phonon temperature increases with the emission of optical phonons and leads to a thermal balance between the phonon and electron systems within 1 ps. After this time frame, there is a hot optical phonon bottleneck, which slows down the carrier cooling process dramatically. Owing to the lack of an anharmonic phonon scattering process, that is, one high-energy optical phonon decomposed into two low-energy acoustic phonons, it is difficult to cool down hot electrons through emission acoustic phonons. This results in an optical phonon energy bottleneck and a long recovery time of THz transmission at low temperature. Figure 9c shows the measured time-resolved THz transmission $\Delta T/T$ for graphene samples with thickness of 14 and 30 layers. Although the thickness of the samples was differed by a factor of two, similar relaxation times of photoexcited charge carriers were obtained in case of the same substrate temperatures.

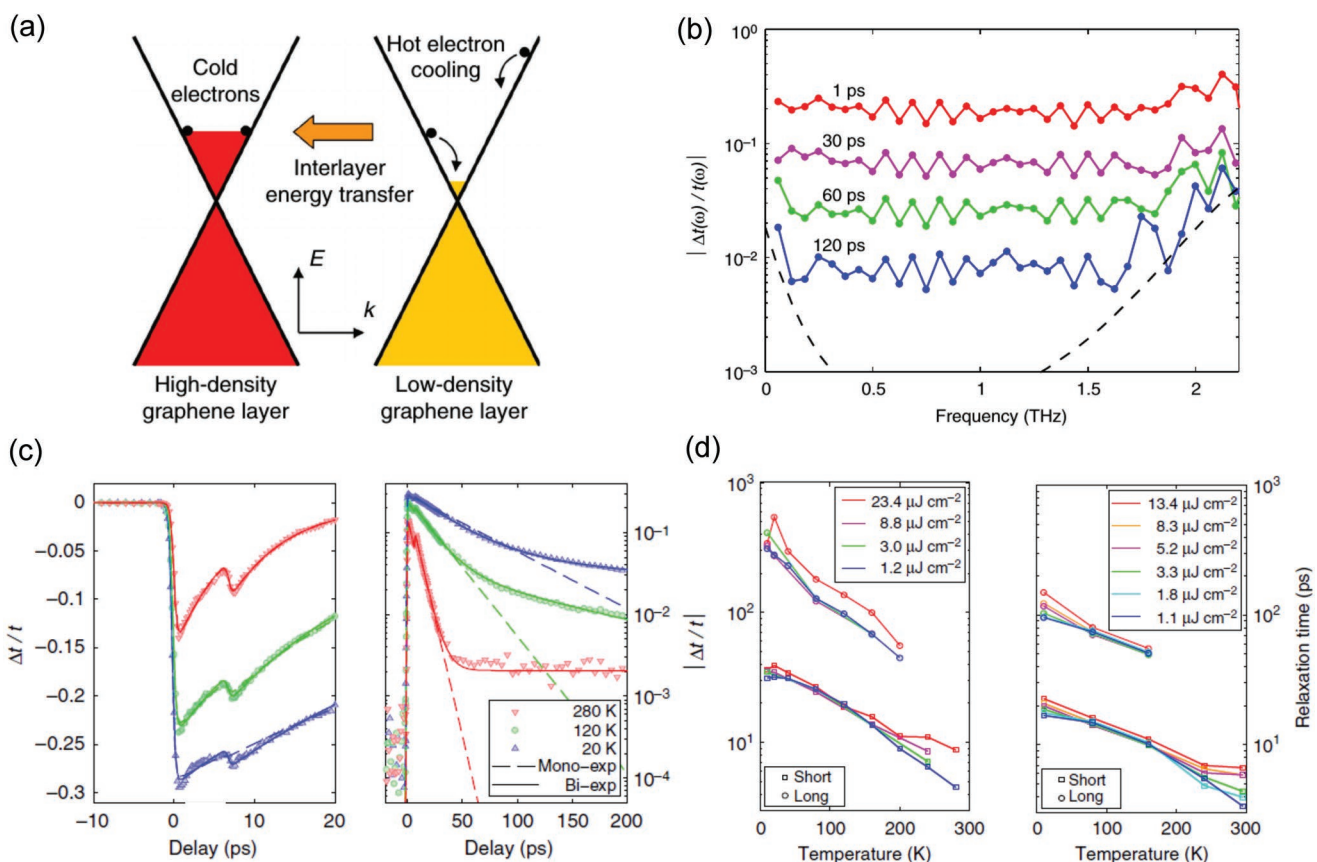


Figure 10. a) Schematic diagram of interlayer Coulombic energy transfer from a hot LD to a cold HD graphene layer. b) Normalized differential THz transmission spectrum with different pump–probe time delays. c) Linear (left) and logarithmic (right) plots of the normalized differential THz transmission as a function of delay time. d) Short and long relaxation times as a function of substrate temperature of multilayer epitaxial graphene samples with thicknesses of 63 (left) and 35 (right) atom layers. a–d) Reproduced with permission.^[113] Copyright 2018, Springer Nature.

In addition to studying the effect of the substrate temperature on the cooling processes of layered graphene, Mihnev et al. performed a joint study by combining theoretical model calculations and optical pump–THz probe spectroscopy to investigate the electronic cooling process in multilayer epitaxial graphene through interlayer Coulomb coupling.^[110] In their study, the multilayer epitaxial graphene samples were deposited on single-crystal 4H-SiC(0001) substrates. By injecting electrons from the interface between the graphene layers and the SiC substrates, the graphene samples were inhomogeneously doped. This led the electron density of graphene layers decreasing from the side closed to the substrate to side of the free space. Graphene layers with high or low electron densities were referred to as the HD or LD layers, respectively. When the graphene sample was photoexcited, electrons were excited to high-energy states to form hot electrons. These hot electrons were then thermalized with the cold electrons within 50 fs to form a separate nonequilibrium electron and hole distribution, as described in refs. [107] and [108]. After the cooling of hot electrons, the nonequilibrium distributed electrons and holes merged together within around 100–200 fs to form uniform electron liquid in each layer. Owing to the weak electron–phonon interaction and phonon-mediated thermal coupling with different layers, the electron temperatures increased layer by layer. This process is schematically

shown in Figure 10a. To monitor the effect of interlayer energy transfer for the cooling process in LD layers, an optical pump–THz probe spectroscopy measurement was performed on the partly doped multilayer epitaxial graphene samples. Since the THz response was dominated by charge carriers in the LD layers, cooling process of these layers induced by their coupling to the HD layers could be extracted. Figure 10b gives the normalized differential THz transmission spectra with various pump–probe time delays. The time-resolved THz transmission at different substrate temperatures is plotted on the linear and the logarithmic scales in the left and right sides of Figure 10c, respectively. As shown in Figure 10c, the carrier relaxation processes can be described by a monoexponential decay line at a temperature of 280 K and by a bi-exponential decay line at 20 K. Moreover, the lifetime of hot carriers decreases with increasing the substrate temperature. The slower relaxation process at low substrate temperature was attributed to the interlayer Coulomb energy transfer between layers with different charge carrier densities. Figure 10d shows the long and short decay times of multilayer epitaxial graphene with 63 layers (left) and 35 layers (right) with different substrate temperatures and excited by laser pulses with various power densities. As indicated in Figure 10d, the relaxation times were very close by varying the pump fluences except at high temperatures. The increase of

the decay time with high pump fluences was explained as the results of the temperature differences between the HD layers and the SiC substrate. In the case the HD layer temperature is higher than that of the substrate, energies in the HD layers will be transferred into the substrate via thermal conduction instead to the LD layers. Moreover, the electron temperature difference between the HD and the LD layers decreases with the increase of the substrate temperature. This also leads to a reduction of the layer energy transfer efficiency. This result indicated that the electron Coulomb interactions between different layers provide an interlayer thermal transport channel, even though both the electron–phonon coupling and phonon-mediated thermal transfer between different layers are very weak.

4.3.2. Carrier and Exciton Dynamics in 2D TMD

Although numerous time-resolved pump–probe measurements have been performed on 2D TMD materials to understand their ultrafast carrier dynamics,^[111–113] most of these studies were performed using optical pump–optical probe frameworks. Performances using optical pump–THz probe spectroscopy have only been investigated in a few reports.^[29,57,114–116] In contrast to the optical pump–optical probe measurements, which monitor the dynamic processes of excitons, optical pump–THz probe spectroscopy is ideal to study the time- and frequency-resolved charge carrier densities, mobilities, and photoconductivities in 2D TMD materials. In 2015, Kar et al. reported a time-resolved optical pump–THz probe measurement to study the dynamics of photoexcited charge carriers in self-supported MoS₂ laminates with different layer numbers.^[57] In their experiment, Kar et al. pumped their MoS₂ laminate sample using a femtosecond 800 nm wavelength laser pulse to excite charge carriers with indirect band structure through phonon assistance. **Figure 11a** gives the transient THz transmission of MoS₂ laminate after the optical excitation. The free charge carriers were initially relaxed within a time of few picoseconds, which was followed by a slow relaxation longer than 570 ps. The fast relaxation process was identified as the result of a defect-assisted Auger process, whereas the slower relaxation process arose when the formed excitons were bound to defects and prevented the defect-assisted Auger process.^[57] Moreover, Kar et al. extracted the complex refractive index of the MoS₂ laminate using THz-TDS and obtained a nearly frequency-independent complex refractive index within the THz band width of 0.5–2.5 THz. The values of the measured refractive index (real part of the complex refractive index) $n \sim 3$ and the extinction coefficient (imaginary part of the complex refractive index) $\kappa \sim 0$, shown in Figure 11a, indicated the MoS₂ laminate exhibited the characteristics of a semiconductor with weak dielectric screening.

Following the pioneering research on the charge carrier dynamics of 2D TMDs, He et al. performed an optical pump–THz probe measurement to study the competition between the relaxation channel of free charge carriers and neutral excitons in layered WSe₂ based on the different THz responses of the free charge carriers and bound excitons.^[117] The measured time-resolved real and imaginary parts of the complex photoconductivities pumped with different power intensities are

shown in Figure 11c. In principle, the real part of the complex photoconductivity describes the THz response of free charge carriers, whereas the imaginary part of the complex photoconductivity corresponds to the bound excitons. As shown in Figure 11c, both the real and the imaginary parts of the photoconductivities increased with pump fluences. The peak values of the complex photoconductivity as a function of the excitation laser power intensity are given in Figure 11d. The nonlinear absorption of free carriers, which corresponds to the real part of photoconductivity, demonstrates strong electron–photon and electron–impurity interactions. In contrast to the nonlinear response of the real part of the complex photoconductivity, the linear response of the imaginary part of photoconductivity indicates strong defect or impurity scattering with bound excitons. A schematic illustration on the relaxation pathways of free charges and bound excitons in layered WSe₂ is given in Figure 11d.

In addition to the work of He et al., a series of investigations have been performed by different research groups^[29,114,115] to investigate the ultrafast dynamics of free carriers and bound excitons in 2D TMDs by monitoring the time evolution of complex photoconductivity. By analyzing the time-dependent complex photoconductivity of 2D TMDs with different layer numbers, the physical principles of free carrier and bound exciton relaxation channels were obtained. Details of their experiments and discussions are reported elsewhere.^[29,114,115]

Based on the different THz responses of free charge carriers, plasma, and excitons at different states (e.g., bright state, dark state, and trapped state), Liu et al. further studied the ultrafast dynamics of the electron–hole gas states within a charged and neutral phases generated by optical excitation in single-layer MoS₂ using optical pump–THz probe spectroscopy.^[116] In their experiments, the time evolution of THz response for MoS₂ with both bulk and single-layer geometry structures were measured under photoexcitations with the wavelengths of the pump pulse at 400 and 800 nm. As shown in **Figure 12a**, a fast decay of around 20 ps along with a slow decay process on the nanoseconds timescale was obtained from the THz response of single-layer MoS₂. To show the different physical principles of the fast (slow) relaxation process, the THz response of free carriers, bright exciton, and long-lived state are schematically illustrated in Figure 12b. In this figure, strong absorption of the unbound electrons and holes resulted in an initial negative differential THz transmission signal around zero delay time. For the bright excitons (process II), the THz field only coupled weakly to these neutral quasiparticles through a nonresonant interaction. For the dark exciton state with energy located in the middle of the bandgap (process III), which corresponded to a trapped exciton with trapping center or scattering with different excitons, the coupling with THz field was even weaker and led to a longer lifetime. The plasma, the bright, dark, and long lived excitons, along with their corresponding positions in the band structures are schematically shown in Figure 12c. Different THz responses of free carriers and exciton states revealed that the fast component of the measured transient THz response corresponds to the lifetime of bound electron–hole pairs, whereas the slow relaxation is induced by the evolution of the trapped or dark exciton states.

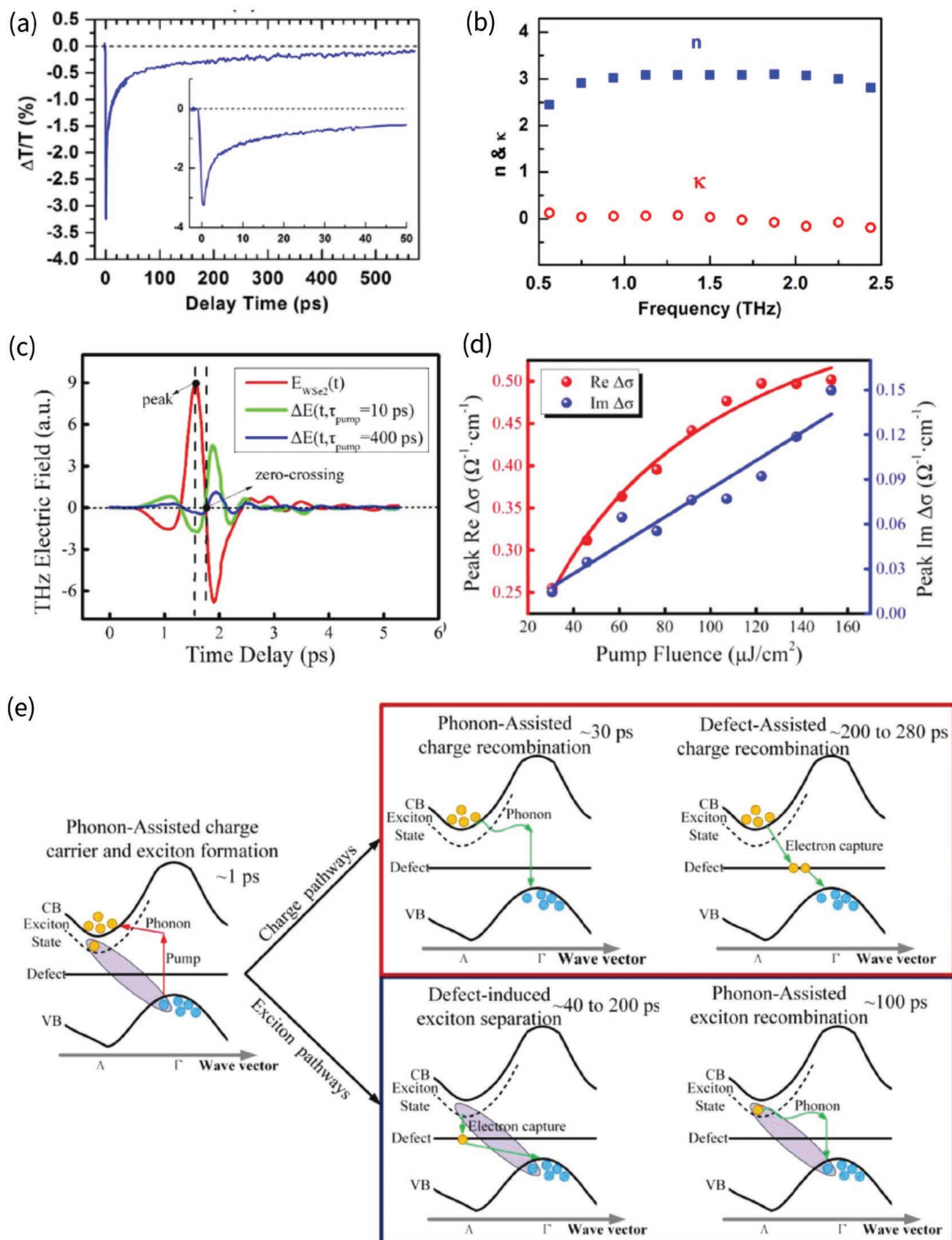


Figure 11. a) Transient THz absorption after photoexcitation by the 800 nm pump. b) Measurement of the real part of complex refractive index n and the imaginary part of complex refractive index κ of the MoS₂ laminate. a,b) Reproduced with permission.^[57] Copyright 2015, American Chemical Society. c) Time-resolved real and imaginary parts of photoconductivity with different pump fluences. d) Real and imaginary parts of the complex photoconductivity as a function of pump fluence with a pump-probe delay time of 0 ps. e) Schematic of relaxation pathways of free charge carriers and bound excitons in layered WSe₂ material. c–e) Reproduced with permission.^[120] Copyright 2014, Wiley-VCH.

5. Transport Properties of 2D vdW Materials

Apart from monitoring the ultrafast dynamics of photo-excited unbound electron-hole pairs and bound excitons,

photoconductivity extracted from THz-TDS itself reveals the transport properties of materials. The transport property, that is, the conductivity of 2D vdW materials is of fundamental importance for optoelectronic devices. In this section, we will

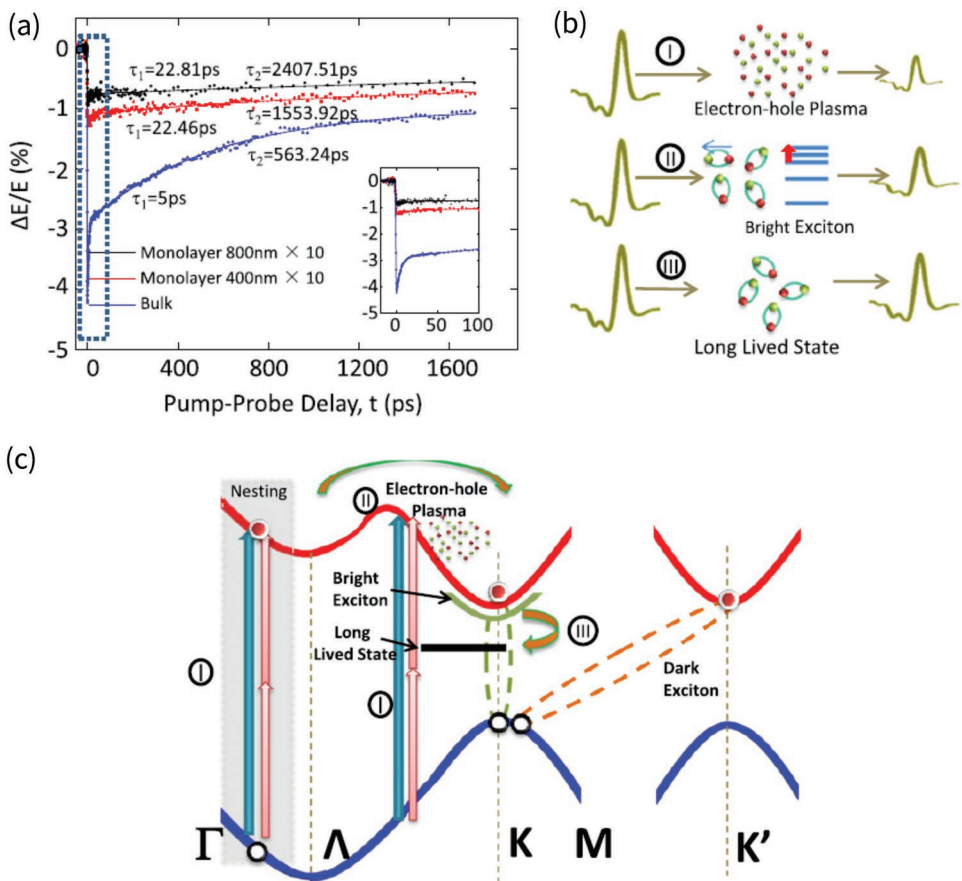


Figure 12. a) Temporal evolution of the transient THz response of monolayer and bulk MoS₂ excited by femtosecond laser pulses with central wavelengths of 400 and 800 nm. b) THz responses of the electron–hole plasma, exciton, and long-lived mid-gap state. c) Schematic illustration of relaxation processes of electron–hole plasma after one- or two-photon excitation. a–c) Reproduced with permission.^[119] Copyright 2012, IOP Publishing Ltd.

discuss the recent progress on the characteristics of charge transfer processes in layered vdW materials obtained from THz-TDS-based measurements.

5.1. Conductivity of Graphene in the Equilibrium State

Studies on the electrical transport properties of layered graphene by noncontact THz-TDS commenced in 2006, which is shortly after the discovery of single-layer graphene.^[118] In this material, the Fermi energy, the carrier density, and the electrical conductivity can be modified by applying gate voltages. In 2012, Maeng et al. reported a THz-TDS study on the nonlinear conductivity of monolayer graphene modified by varying the applied gate voltage.^[119] In their experiments, Maeng et al. shifted the Fermi energy of graphene by changing the bias in the range of -50 to 50 V. The shift of Fermi energy along with its corresponding frequency-resolved sheet conductivity under various gate voltages is given in Figure 13a. As indicated in Figure 13a, the Fermi energy shifted from the conduction band to the valence band, i.e., crossing the Dirac point by varying the bias from +45 to -20 V, which increased the carrier density. Moreover, it can be seen from Figure 13a that a dispersionless sheet conductivity appears with frequency of THz field lower

than 1THz. This result corresponds to the broadening of the Drude scattering process. Figure 13b gives the average sheet conductivity of monolayer graphene with various bias voltages, which corresponds to the shift of the Fermi energy. The shaded area of Figure 13b gives the fitting curves obtained from Drude model using scattering time between 32 and 39 fs. In the high carrier density region (gate voltage V_g below -25 V), where the Fermi energy was far below the Dirac point, the sheet conductivity decreases slowly with the increasing gate bias and was identified to change with the square root of the carrier density. With the increase of the Fermi energy (gate voltage V_g between -25 and 25 V), the sheet conductivity decreases rapidly with the bias voltage and was identified to be dominated by the dense hole plasma. By further increasing the gate bias (gate voltage V_g above 25 V), the Fermi energy was shifted slightly above the Dirac point. In this case, the sheet conductivity remained constant with bias and was identified to be dominated by the impurities or trap charges.

In addition to the work of Maeng et al., Buron et al.^[120] performed ultra-broadband THz-TDS measurements to investigate the role of substrates on charge transfer processes in monolayer graphene. In their experiments, the THz response covered the frequency range up to 15 THz. Two types of monolayer graphene were measured in the experiments: one was grown on

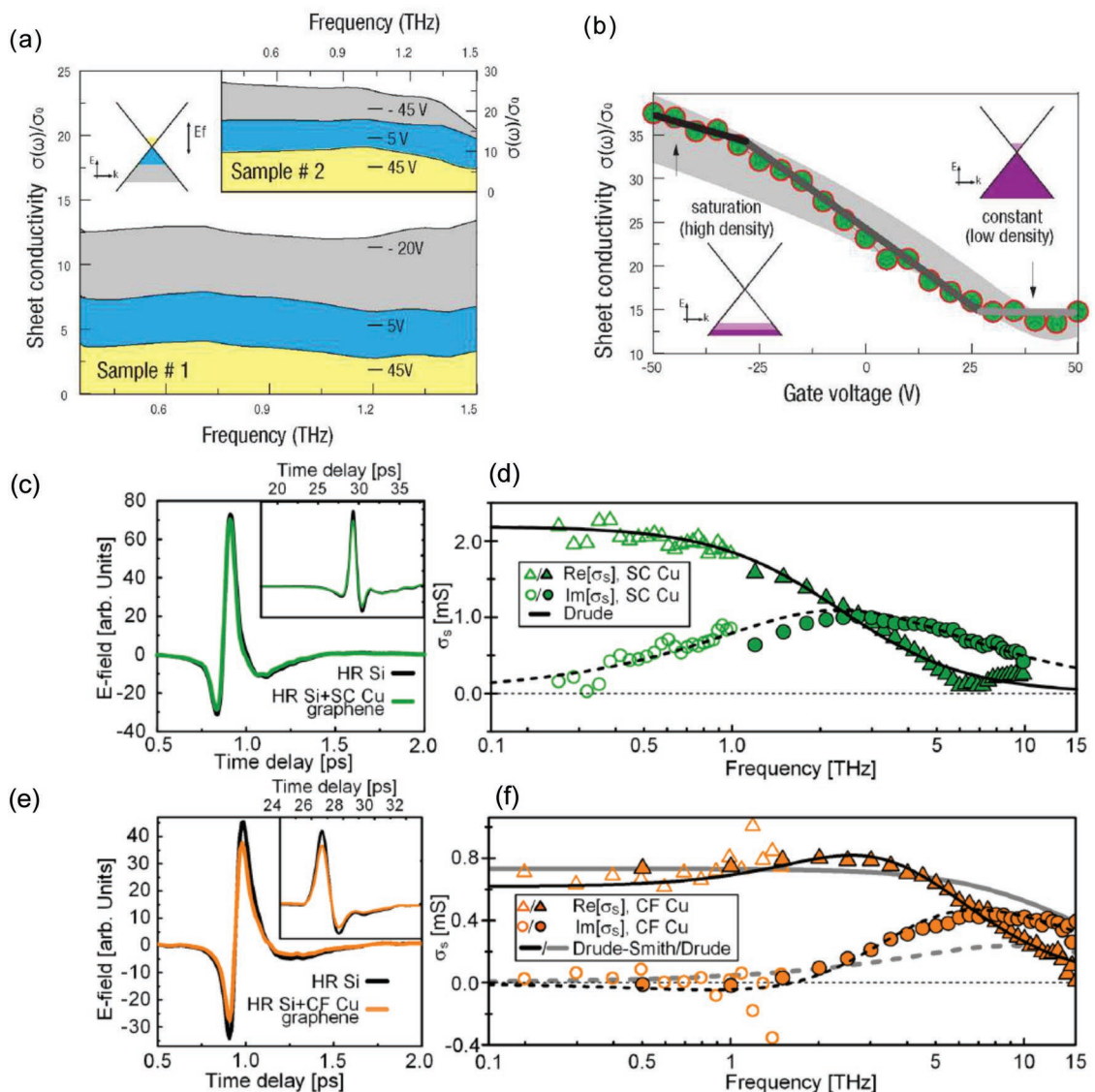


Figure 13. a) Frequency-resolved sheet conductivity of monolayer graphene measured at gate biases of -20, 5, and 45 V for sample #1 and measured at gate biases of -45, 5, and 45 V for sample #2. b) Average sheet conductivity as a function of gate voltage. a,b) Reproduced with permission.^[122] Copyright 2010, American Chemical Society. c,e) THz-TDS measured time-domain waveforms of HR-Si substrate, SC copper-grown graphene, and CF copper-grown graphene. d,f) Real (triangles) and imaginary (circles) parts of frequency-resolved conductivity of SC and CF copper-grown graphene. Fitting curves using the Drude model for SC copper-grown graphene are given as solid (real part) and dashed (imaginary part) lines; fitting curves using the Drude-Smith/Drude model for FC copper-grown graphene are given as black/gray solid (real part) and dashed (imaginary part) lines. c-f) Reproduced with.^[123] Copyright 2017, American Chemical Society.

the single crystal (SC) copper while the other was deposited on the commercial foil (CF) copper by using the CVD approach. After growth on different coppers, the graphene layers were transferred to SiO_2 flakes, which were grown on high resistivity silicon. Time-resolved waveforms of the transmitted THz pulses for graphene samples deposited on SC copper with high-resistivity silicon substrate, on CF copper with high-resistivity silicon substrate, along with the transmitted THz pulses for a clean high-resistivity silicon substrate as reference are given in Figure 13c,d. The real and the imaginary parts of the complex conductivities of graphene layers deposited on the SC copper and CF copper are presented in Figure 13e,f, respectively. The ultrabroadband THz-TDS conductance spectrum shows that

the classical Drude model gave a good description on the transport properties of SC copper-grown graphene film, whereas the transport processes of CF copper-grown graphene obey the Drude-Smith model, respectively. Comparing to the standard Drude model, an additional backscattering term was introduced to modify the standard model to characterize the effects of a certain extent of localization. This result indicated that the microscopic electrical discontinuity exists in graphene samples grown CF copper. Moreover, this characteristic provides a possible way to monitor the quality of graphene layers by using THz-TDS.

In contrast to monolayer graphene with a simple crystal structure, bilayer graphene is a 2D vdW structure composed

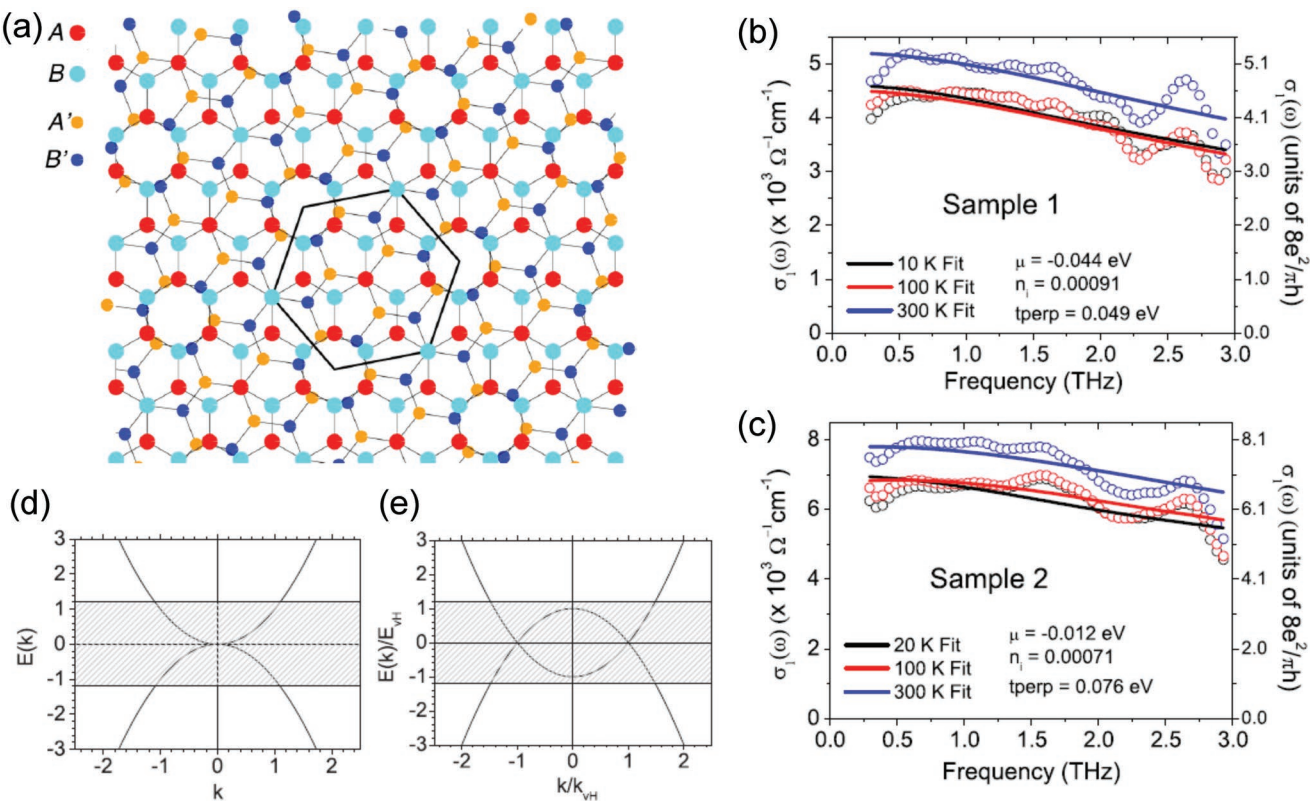


Figure 14. a) Atomic arrangement of atoms in bilayer graphene with a twisting angle of 21.8° . A (A') and B (B') are the sublattices of the first (second) layer. b,c) Real part of conductivities of bilayer graphene of samples 1 and 2 extracted from THz spectrum (circles) and simultaneous fits using the Drude-like model (solid lines). d,e) Schematic dispersions of a Bernal and twisted bilayer graphene, respectively. The shaded region indicates the states which are broadened by disorder in the sample. a–e) Reproduced with permission.^[64] Copyright 2013, American Physical Society.

by two single layers of graphene with a certain rotation angle between adjacent layers. Compared with single-layer graphene with only two nonequivalent lattice sites (A and B), the non-equivalent lattice site of bilayer graphene is more complicated. In the most common case of bilayer graphene, the adjacent layers are rotated by 60° , and this type of bilayer graphene is known as Bernal-stacked bilayer graphene. In contrast to Bernal-stacked bilayer graphene, bilayer graphene fabricated by CVD tends to form a spiral shape geometry structures, that is, a rotation through a twisting angle θ between two graphene layers as a Moire pattern on the surfaces. Bilayer graphene with a twisting angle of $\theta = 21.8^\circ$ is illustrated in Figure 14a. In this case, hopping between different A sites of double-layer graphene requires an energy of t_\perp for each electron and this leads to different transport properties in such systems. To understand the temperature- and disorder-dependent transport properties of twisted bilayer graphene, Zou et al. performed time-resolved THz spectroscopy measurements to investigate the frequency-resolved conductivity in twisted bilayer graphene at temperatures of 10–300 K.^[64] The real part of the frequency-resolved complex conductivity of two bilayer graphene samples extracted from the THz response spectrum, along with their corresponding fitting lines based on the Drude-like model at different temperatures, are presented in Figure 14b,c. As shown in Figure 14b,c, the complex conductivity of bilayer graphene followed the Drude-like model by considering the effects of

disorders except for the strong conductivity spectral amplitude located at around 2.7 THz. This conductivity peak was explained as the result of the van Hove singularity-induced density of state enhancement. Figure 14d,e show that the transport properties of twisted bilayer graphene can be described by using the Bernal bilayer graphene model with a smaller value of hopping energy correction.

5.2. Conductivity of Photoexcited Graphene

Layered graphene is a gapless 2D vdW material, which exhibits the physical properties of high Fermi velocity with high in-plane charge carrier mobility.^[1–3] These characteristics enable the high-quality layered graphene to exhibit high sheet conductivity even without photoexcitation. However, owing to the linear electronic dispersion relation of layered graphene around the K point in BZ, this material shows attractive electronic and optical properties, such as strong light absorption over a broad spectral range and pronounced optical response.^[121,122] To investigate the photoconductivity of layered graphene, a series of time-resolved THz spectroscopy measurements with photoexcitation have been performed on CVD-grown single-layer graphene with optically transparent substrates.^[77,123,124]

In 2013, Jnawali et al. reported a THz-TDS measurement on the frequency-resolved sheet conductivity of CVD-grown

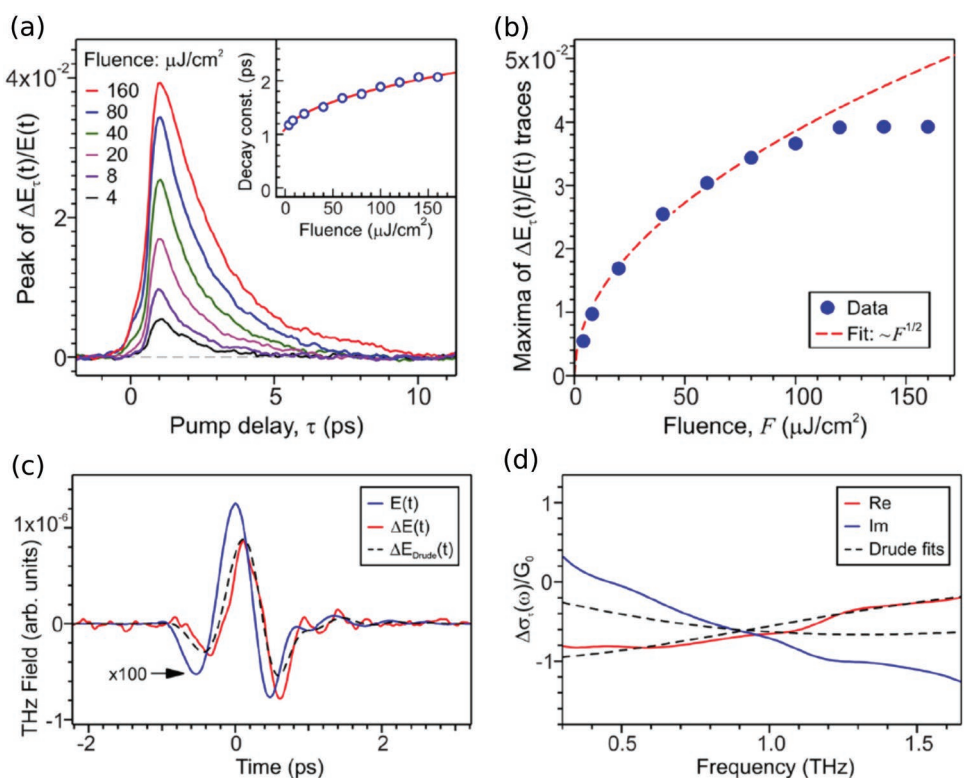


Figure 15. a) Time-resolved THz response $\Delta E_\tau(t)/E(t)$ of graphene layer pumped with various power intensities. b) Maxima values of $\Delta E_\tau(t)/E(t)$ as a function of pump fluence. c) Photoinduced change in the THz transmission with a pump power intensity of $20 \mu\text{J}/\text{cm}^2$ and a time delay of 2.5 ps. d) The photoinduced change of frequency-resolved complex photoconductivity. a–d) Reproduced with permission.^[128] Copyright 2014, American Physical Society.

graphene in conjunction with a femtosecond optical excitation.^[125] In contrast to the increased photoconductivity obtained in the photoexcited multilayer epitaxial graphene,^[107] a rapid decrease of photoconductivity within a few of picoseconds was observed in single-layer graphene grown by CVD. This response was obtained by measuring the transient THz transmission at different pump–probe time delays. The differential transmitted THz field at a certain delay time τ is written as $\Delta E_\tau(t) = E_\tau(t) - E(t)$, with $E(t)$ being the transmitted THz waveform without optical pump and $E_\tau(t)$ the transmitted THz waveform obtained with a time delay of τ after photoexcitation. Figure 15a shows the normalized time-resolved change of transmitted THz waveforms. Compared with the optically pumped THz response of multilayer epitaxial graphene,^[107,108] a negative photoconductivity lasted for a few picoseconds was obtained in the CVD-grown single-layer graphene. As shown in Figure 15a,b, both the intensity and the persisting time of the negative THz photoconductivity increased with power intensity of the excitation laser pulse. To further investigate the relaxation processes of the photoexcited graphene, the measured time-resolved THz response (blue and red solid lines) with a 2.5 ps time delay after photoexcitation on the graphene sample with a power intensity of $20 \mu\text{J}/\text{cm}^2$ along with its corresponding fitting curves (black dashed line) from the Drude model is presented in Figure 15c. As shown in this figure, an enhancement of the THz transmission after photoexcitation in single-layer graphene can be well described by using the simple Drude analysis. A negative change of the real part of the complex photoconductivity

presented in Figure 15d provides a direct proof of the negative THz photoconductivity of CVD-grown single-layer graphene. Jnawali et al. explained their observed negative THz photoconductivity $\sigma(\omega)$ via the Drude response model $\sigma(\omega) = D/\pi(\Gamma - i\omega)$, where D is the Drude weight and Γ is the average scattering rate. The values of D and Γ were closely related to the density and mobility of charge carriers, respectively. The values of these quantities were extracted from the measured THz response spectrum. After photoexcitation, a more significant increase of the scattering rate than the Drude weight within a few picoseconds resulted in the observed negative photoconductivity.

At almost the same time, Tielrooij et al. performed an optical pump–THz probe spectroscopy measurement to investigate the ultrafast dynamics of photoexcited charge carriers of CVD-grown layered graphene samples with electron doping.^[126] In their experiments, graphene samples were excited by photons with energies between 0.16 and 4.65 eV. The time-resolved pump-induced change in THz transmission $\Delta T/T_0$ along with the peak values of $\Delta T/T_0$ are shown in Figure 16a,b as a function of absorbed photodensity. As shown in Figure 16a, the temporal evolution of $\Delta T/T_0$ was nonmonotonic. The differential transmission $\Delta T/T_0$ first increased after photoexcitation and reached its peak value at a time delay of 0.2 ps. Following the rapid increase of the THz transmission, the value of $\Delta T/T_0$ decreased subsequently within a time of 1.4 ps. In the former process, scattering between photoexcited charge carriers and the unexcited cold electrons with energy below the Fermi energy promoted the low-energy carriers to be above the

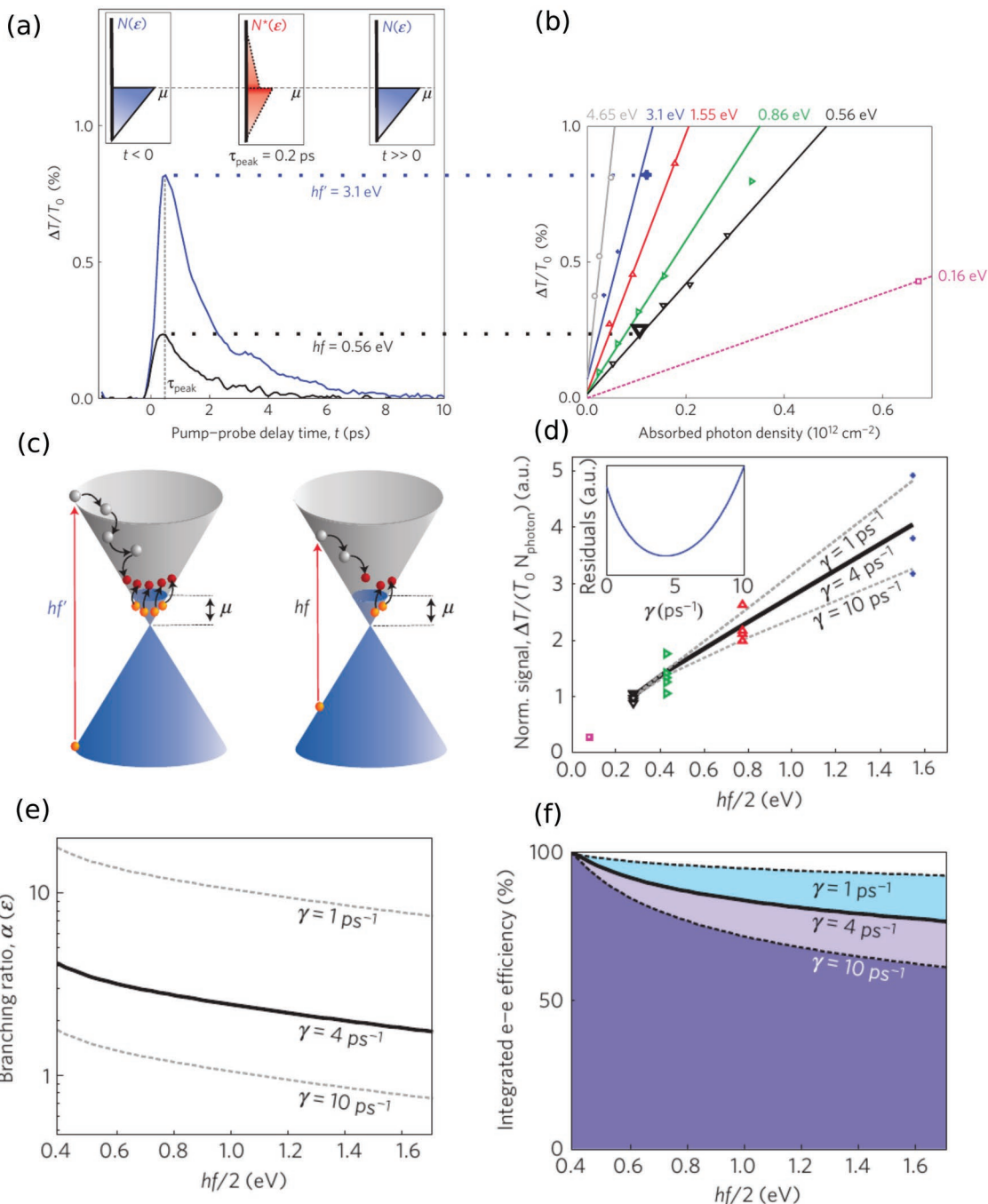


Figure 16. a) Time-resolved THz response of graphene layer excited by laser pulses with two different photon energies. b) Scaling of the differential transmission signal $\Delta T/T_0$ peak values as a function of absorbed photon density. c) Schematic illustration of the energy cascade of doped graphene after photon excitation by different pump wavelengths. d) The differential transmission signal $\Delta T/T_0$ peak value normalized by absorbed photon density as a function of initial carrier energy. e) The branching ratio between carrier–carrier scattering and optical-phonon emission as a function of initial carrier energy. f) The integrated efficiency for the carrier–carrier scattering pathway as a function of initial carrier energy. γ is the electron–phonon coupling constant value. a–f) Reproduced with permission.^[129] Copyright 2017, Springer Nature.

Fermi level (heating the cold electrons). In the latter process, the photoexcited carriers and the hot carriers heated by the scattering process relaxed to the ground state through an electron–lattice interaction with a longer time scale (1.4 ps). Figure 16b shows that the peak value of $\Delta T/T_0$, which corresponded to the concentration of photoexcited and heated hot carriers,

increased with the increases of pump photon energy and power intensity. The effects of photon energy on the peak value of $\Delta T/T_0$ are shown schematically in Figure 16c. Here, the higher-energy photons resulted in a much higher carrier–carrier scattering probability during the relaxation cascade. This led to a higher average electron temperature and stronger negative

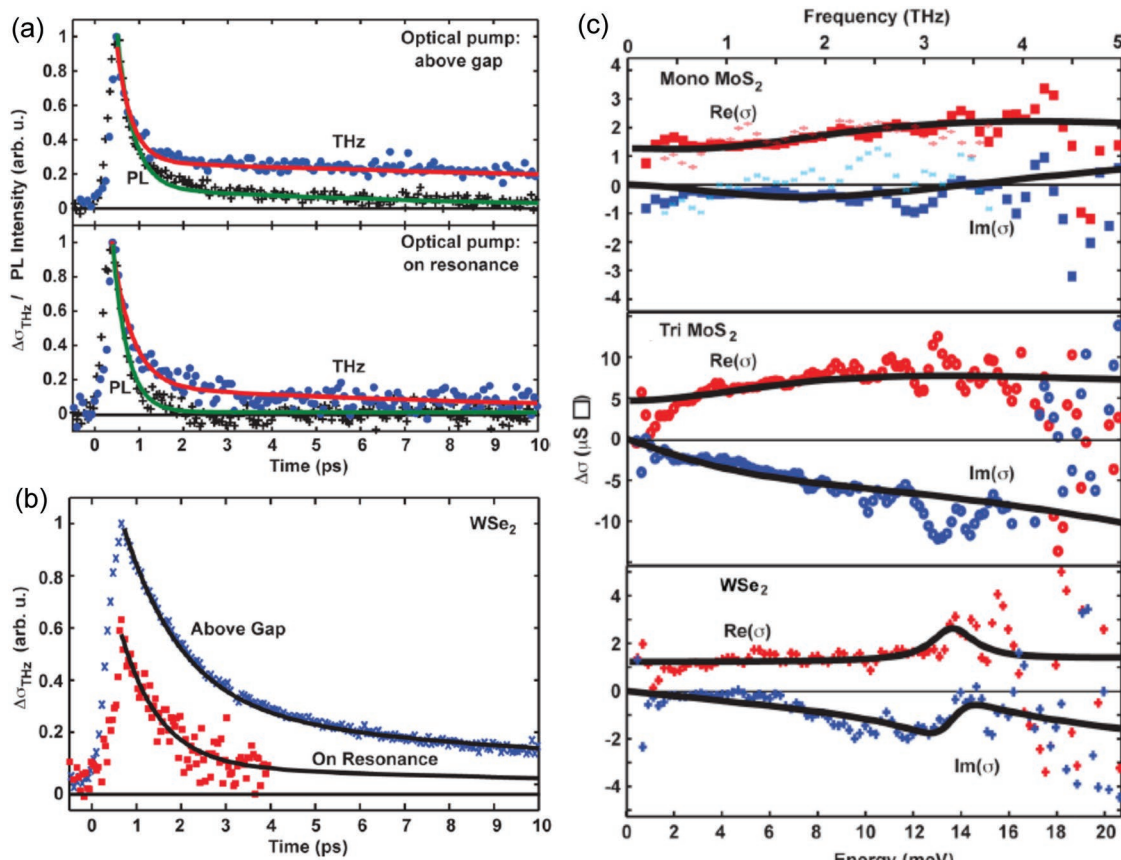


Figure 17. a) Photodynamics of monolayer MoS₂ measured by optical pump–THz probe spectroscopy (blue circles) and PL upconversion spectroscopy (black crosses) excited by an above gap optical pump (upper panel) and an on resonance optical pump (lower panel). b) Normalized THz photoconductivity of monolayer WSe₂. c) Frequency-resolved complex THz photoconductivity of monolayer MoS₂ (upper panel), trilayer MoS₂ (middle panel), and monolayer WSe₂ (lower panel). The real and the imaginary parts of the complex photoconductivity are color-coded in red and blue, respectively. a–c) Reproduced with permission.^[131] Copyright 2012, American Chemical Society.

photoconductivity. Moreover, Tielrooij et al. determined the normalized $\Delta T/T_0$ peak value by the absorbed pump power intensity, the branching ratio between electron–electron scattering and electron–phonon interaction, and the integrated carrier–carrier scattering efficiency of the optical pumped graphene sample with various initial carrier energies. These results are shown in Figure 16d–f. Three electron–phonon coupling strength values, $\gamma = 1, 4$, and 10 ps^{-1} were used to simulate the experimental results. Among these coupling strength parameters, $\gamma = 4$ resulted in the best fitting, whereas $\gamma = 1$ and 10 illustrated the cases with weaker and stronger electron–phonon coupling, respectively. Figure 16d–f indicates that the carrier–carrier scattering dominates the relaxation process of photoexcited charge carriers, especially with lower initial carrier energy.

In the same year, Frenzel et al. also reported a similar reduced absorption of THz radiation in photoexcited graphene layers, which corresponded to a negative THz photoconductivity.^[127] In contrast to Tielrooij et al.,^[126] they attributed their observed negative THz photoconductivity to the thermal broadening of the electron distribution induced by both photoexcitation and strong electron–phonon coupling in the graphene sample and the substrate. These three works indicated the existence of a negative THz photoconductivity in electron-doped single-layer

graphene fabricated using the CVD approach. However, what the physical principles are of such negative photoconductivity is still an open question for scientists.

5.3. Photoconductivity of 2D TMD

In contrast to gapless graphene with linear electronic band dispersion relation around K point in BZ, monolayer (or multi-layer) 2D TMDs are semiconductors with direct (or indirect) band structures along with a reduced dielectric screening and strong spin–orbit interactions. These characteristics result in the different transport mechanisms of photoexcited 2D TMDs compared to layered graphene. The pioneering work of an optical pump–THz probe study on the photoconductivity in 2D TMD was performed by Docherty et al. in 2014.^[128] In this work, they studied the ultrafast transient THz conductivity of CVD-grown monolayer TMDs using time-resolved PL spectroscopy and THz-TDS. The measured time-resolved PL intensity and the THz photoconductivity of monolayer MoS₂ excited by the above gap and on resonance pump pulses are given in Figure 17a. As shown in this figure, both PL intensity and the THz photoconductivity of single-layer MoS₂ quench

rapidly after photo excitation. Moreover, this rapid quenching was independent of whether resonantly created excitons or hot electron-hole pairs were involved. Docherty et al. explained this fast quenching to the fast surface trapping process, interaction between surface and substrate, and/or extrinsic charge carrier-mediated recombination. Figure 17b gives the normalized THz photoconductivity of monolayer WSe₂ excited by the above gap (blue crosses) and on resonance (red squares) pump pulses. Comparing Figure 17a with Figure 17b, we see that both the rise and the relaxation times of the WSe₂ sample were slower than those of MoS₂. A full understanding of this difference is still unclear, and further theoretical efforts are needed. The full photoconductivity spectrum of monolayer WSe₂ taken with a 1.0 ps photoexcitation is presented in Figure 17c. In this figure, the real and imaginary parts of the complex photoconductivities are plotted as red and blue symbols, respectively. All of these samples appeared with weak response on free charge carriers and strong Lorentzian resonances. This result indicated a small component of the free charge carriers existed with bound excitons. Compared with the single-layer 2D TMD samples, trilayer MoS₂ showed a resonance of the photoconductivity with energy much larger than the experimental bandgap. This result suggested a large exciton binding energy in trilayer MoS₂.

To investigate the effects of bound and unbound electron-hole pairs for time evolution of the photoconductivity in multi-layer TMDs, Xing et al. performed optical pump–THz probe spectroscopy studies on a large-area CVD-grown WS₂ laminate with few-layer structure.^[129] In their experiments, the samples were excited using laser pulses with a wavelength centered at 400 nm and the carrier dynamics were probed by using THz-TDS. The measured THz transmission $E_{\text{ref}}(t)$ and the photo-modulated THz waveform $\Delta E(t)$ are plotted in Figure 18a. Figure 18b provides the change of complex sheet conductivities with various pump–probe time delay. Both the real and imaginary parts of the conductivities reached their peak (or valley) values at around 4 ps, which indicated the formation of bound excitons from photoexcited free charge carriers within 4 ps. Moreover, the relaxation time of the real part of the photoconductivity was significantly longer than that of the imaginary part. This result indicated a shorter lifetime of the exciton than the mobile charge carriers. The real and imaginary parts of the time-resolved photoconductivities with different pump fluences are presented in Figure 18c,d, respectively. As shown in these figures, a stronger THz response corresponded to higher pump power intensity. The frequency-resolved complex pump-induced change in sheet conductivities with various pump fluences and measured at different pump–probe delay times are presented in Figure 18e,f, respectively. The conductivities extracted from THz-TDS measurements are plotted as blue squares (real part) and red circles (imaginary part), whereas the fitting curves using the Drude–Lorentz model are given in blue and red solid lines. As shown in Figure 18e,f, the measured photoconductivities agree well with the fitting curves obtained from the Drude–Lorentz model. This result indicated that the transport process of the photoexcited few-layer WS₂ film was dominated by the unbound free charge carriers instead of bound excitons.

In addition to the negative THz conductivity observed in graphene samples fabricated using CVD approach, Lui et al.

reported negative photoconductivity in CVD-grown monolayer MoS₂ from their optical pump–THz probe spectroscopy measurements.^[130] The CVD-grown monolayer MoS₂ samples presented the n-doped characteristics.^[131,132] In their experiment, the monolayer MoS₂ sample was excited by pump pulses with a wavelength of 400 nm. The transmitted THz waveforms with $[\Delta E(t, \tau)]$ and without $[E(t)]$ photoexcitation were obtained using THz-TDS. The measured time-resolved normalized THz waveform is given in Figure 19a. The measured THz response exhibited a fast relaxation time around 1 ps, followed by a slow relaxation of around 42 ps. Figure 19b shows the change of complex conductivity of monolayer MoS₂ with time delays between the excitation and the THz probe pulse for 3 and 40 ps. The real and the imaginary parts of the complex photoconductivities are given in red and green colors, respectively. As shown in Figure 19b, both the real and imaginary parts of the change of conductivity were negative. To understand the physical principles of the negative photoconductivity, the excitonic and trionic effects on the THz response are schematically illustrated in Figure 19c. In monolayer TMDs, the excessive free electrons can be captured by charge neutral excitons within time of 1 ps and forming bound three-particle states with negative charges when an excess of doped electrons are available. These charged three-body bound states are referred to as trions, with similar transport properties to free charge carriers except heavy effective mass and reduced mobility.^[133] These characters lead to a negative photoconductivity of monolayer MoS₂. To further investigate the mechanism of trion, Lui et al. performed optical pump–THz probe measurements on monolayer MoS₂ samples by varying the pump fluences, the pump photon energy, and the chemical doping stages, as shown in Figure 19d,f. All of these experiments indicated that trion formation led to the reduction of the THz conductivity by increasing the effective mass and reducing the carrier mobility.

6. Summary and Outlook

In summary, the time-resolved ultrafast THz spectroscopy with or without photoexcitation is a powerful tool to monitor the nonequilibrium evolution of free electrons or charged quasiparticles for investigating the ultrafast dynamics of charge carriers in semiconductor nanostructures. Comparing with the other time-domain spectroscopy techniques such as ultrafast transient absorption spectroscopy, optical pump–optical probe measurement, and time-resolved photoluminescence spectroscopy, which also have the ability to measure ultrafast carrier dynamics, only time-resolved THz spectroscopy can provide the time- and frequency-resolved complex photoconductivity of samples. This enables us to extract the time-resolved fundamental physical properties, such as scattering time, density, and mobility of charge carriers. In this review, we provide a brief summary for recent progress on ultrafast carrier dynamics of 2D vdW materials investigated using time-domain THz spectroscopy with or without photoexcitation. After introducing the background of the time-resolved THz spectroscopy technique and a brief overview of the crystal structure, fabrication methods, band structures, and optical properties of 2D vdW materials, we first review monitoring

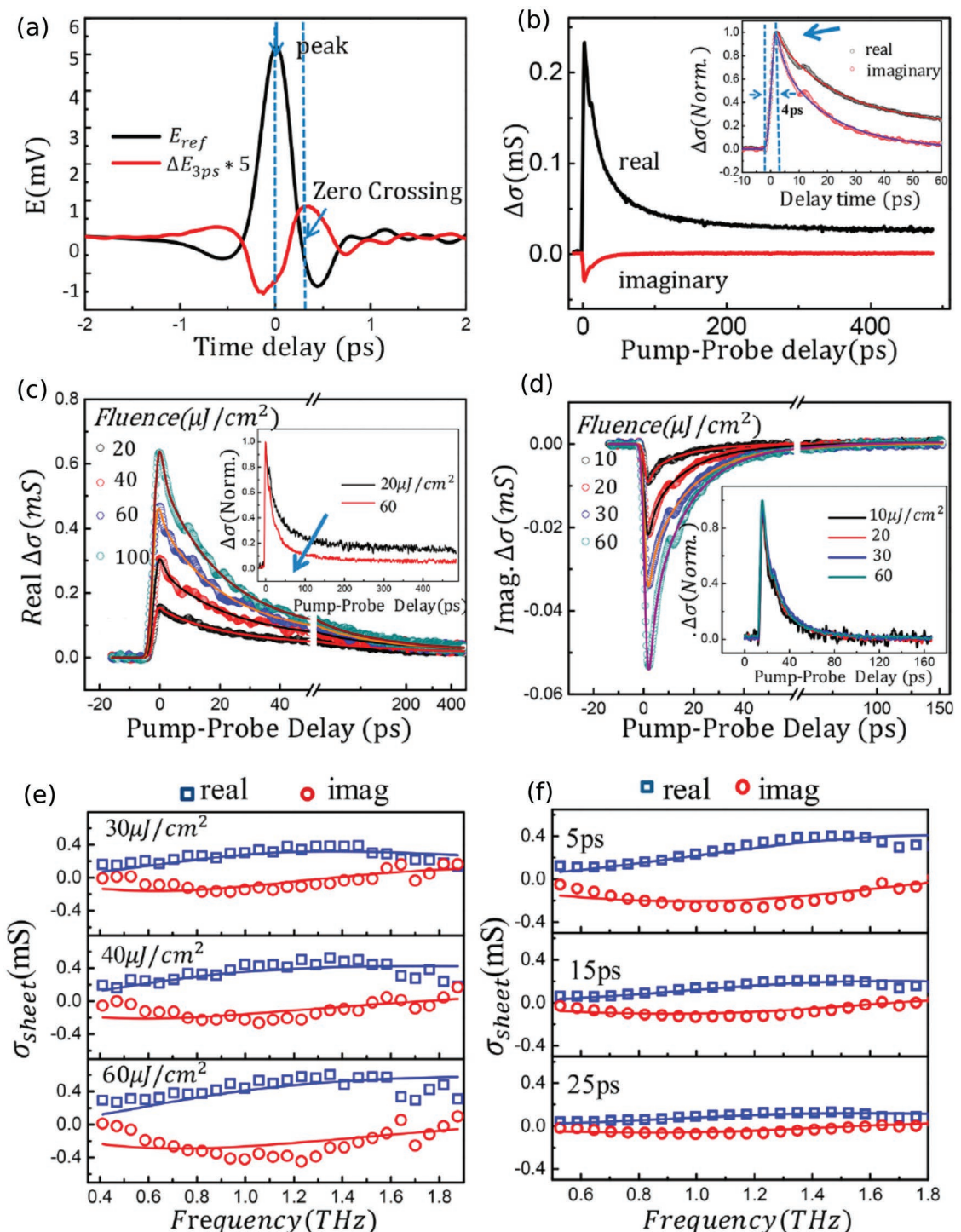


Figure 18. a) Measured THz transmission $E_{ref}(t)$ and the photomodulation of the THz waveform $\Delta E(t)$ in a few-layer WS₂ film. b) Time-resolved change of complex THz conductivity after photoexcitation. c,d) The real part and the imaginary part of the change in complex THz conductivity after an optical pump with various fluences. e) Complex frequency-resolved photoconductivity of WS₂ film measured with a pump–probe time delay of 3 ps and pumped at various fluences. f) Complex frequency-resolved photoconductivity of WS₂ film pumped with a fluence of 50 $\mu J/cm^2$ and measured with various pump–probe time delays. a–f) Reproduced with permission.^[132] Copyright 2014, American Chemical Society.

the formation and relaxation processes of excitons in semiconducting 2D materials and the relaxation of hot electrons in graphene using optical pump–THz probe spectroscopy. Subsequently, we summarize the THz-TDS measured complex

conductivity in graphene at the equilibrium state and the change of complex conductivity under photoexcitation in both graphene and 2D TMDs. In contrast to other materials, negative photoconductivities were obtained in CVD-grown

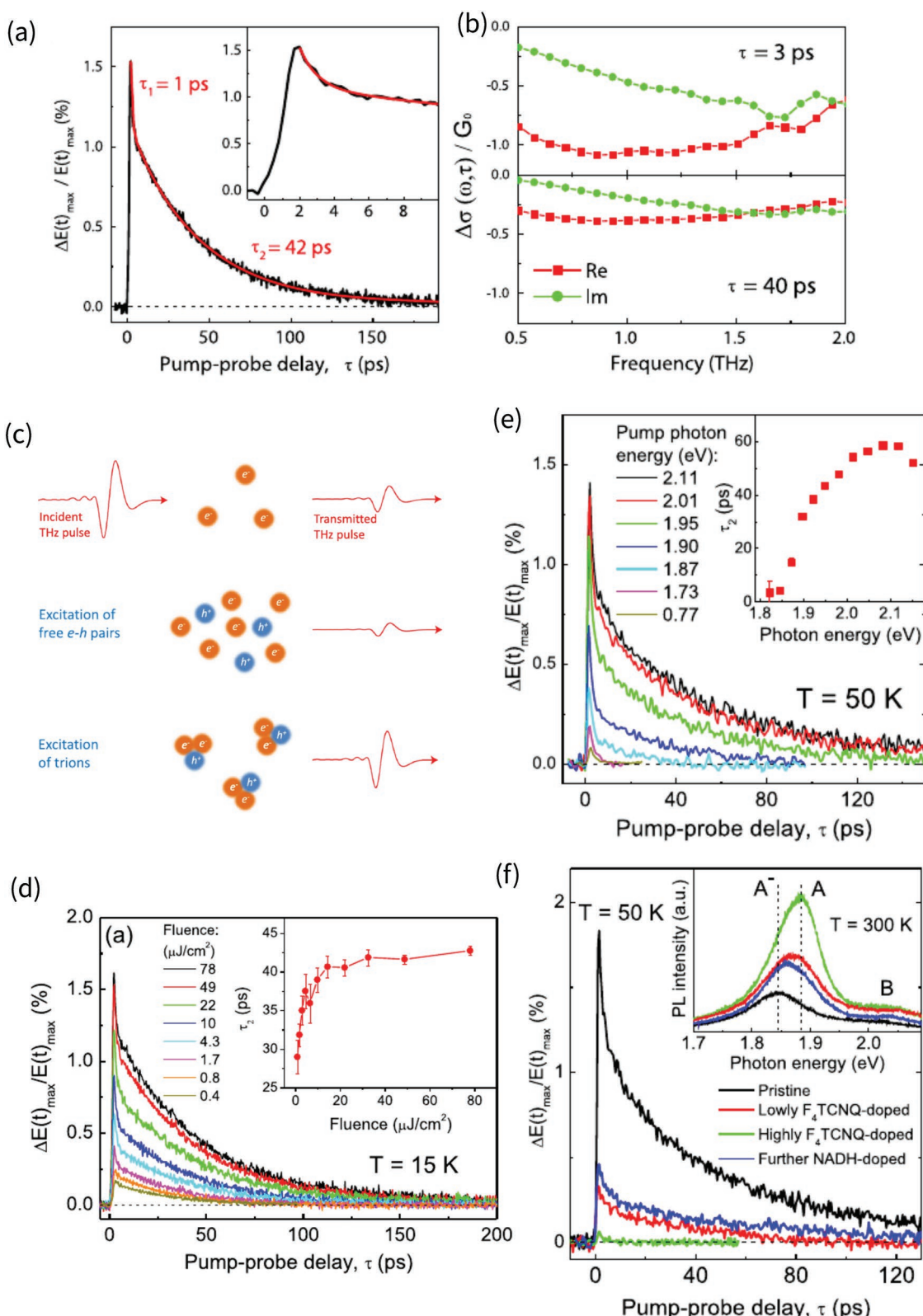


Figure 19. a) Temporal evolution of the ratio between the maximum values of waveforms $\Delta E(t)_{\max}/E(t)_{\max}$. b) The pump-induced change in complex sheet conductivity with a pump–probe time delay of 3 ps (upper panel) and 40 ps (lower panel). c) Schematic of trionic effect on the THz response under photoexcitation. d–f) Time-resolved $\Delta E(t)_{\max}/E(t)_{\max}$ with various pump fluences, pump photon energy, and chemical doping stages, respectively. a–f) Reproduced with permission.^[133] Copyright 2001, American Physical Society.

single-layer graphene and MoS₂ samples. The negative photoconductivity in monolayer MoS₂ was explained as the results of the formation of trions with lower mobility, although the physical principles of negative photoconductivity in graphene are still under debate.

Despite the success of the time-resolved THz spectroscopy technique in the application of monitoring the ultrafast carrier dynamics in 2D vdW materials, there are still many challenges facing further studies. First, the mechanism of neutral and charge bound-exciton formation in 2D semiconductors, which results in a negative or positive photoconductivity, and different carrier and exciton dynamics in TMDs is still not fully understood. In addition, although numerous THz-TDS and optical pump–THz probe studies have been performed on carrier dynamics in graphene, studies on pump-induced ultrafast dynamics processes in 2D TMDs and other novel 2D semiconductors, such as black phosphorus, are still lacking. Moreover, time-resolved THz spectroscopy studies on the carrier dynamics in 2D vdW heterostructures are almost nonexistent. Understanding the ultrafast dynamics process of photoexcited charge carriers in 2D heterostructures is essential for designing 2D optoelectronic devices. Last, but not least, the state-of-the-art time-resolved THz spectroscopy based studies are only focused on the carrier relaxation process and transport properties of 2D materials. The frequency region of THz spectroscopy, which covers the energy of lattice vibrations in 2D materials, is well suited to investigate the phonon resonances or phonon-assisted optical transition processes. Further studies using the techniques of THz pump–THz probe and THz pump–optical probe on 2D vdW materials to investigate the contributions from lattice vibration on the electronic and optical properties of these materials are indeed needed.

Acknowledgements

This work was supported by the National Natural Science Foundation of China (Grant Nos. 11774243, 11774246, 11404224, and 11474206), Youth Innovative Research Team of Capital Normal University (008/19530050146), Capacity Building for Science & Technology Innovation—Fundamental Scientific Research Funds (008/19530050170, 008/19530050180, 008/18530500186, and 025185305000/142), and Scientific Research Base Development Program of the Beijing Municipal Commission of Education.

Conflict of Interest

The authors declare no conflict of interest.

Keywords

2D materials, pump–probe, terahertz spectroscopy, time-resolved, ultrafast dynamics

Received: March 29, 2019

Revised: July 7, 2019

Published online: August 16, 2019

- [1] K. S. Novoselov, A. K. Geim, S. V. Morozov, D. Jiang, Y. Zhang, S. V. Dubonos, I. V. Grigorieva, A. A. Firsov, *Science* **2004**, *306*, 666.
- [2] K. S. Novoselov, D. Jiang, F. Schedin, T. J. Booth, V. V. Khotkevich, S. V. Morozov, A. K. Geim, *Proc. Natl. Acad. Sci. USA* **2005**, *102*, 10451.
- [3] A. K. Geim, I. V. Grigorieva, *Nature* **2013**, *499*, 419.
- [4] S. Z. Butler, S. M. Hollen, L. Y. Cao, Y. Cui, J. A. Gupta, H. R. Gutierrez, T. F. Heinz, S. S. Hong, J. X. Huang, A. F. Ismach, E. Johnston-Halperin, M. Kuno, V. V. Plashnitsa, R. D. Robinson, R. S. Ruoff, S. Salahuddin, J. Shan, L. Shi, M. G. Spencer, M. Terrones, W. Windl, J. E. Goldberger, *ACS Nano* **2013**, *7*, 2898.
- [5] G. R. Bhimanapati, Z. Lin, V. Meunier, Y. Jung, J. Cha, S. Das, D. Xiao, Y. Son, M. S. Strano, V. R. Cooper, L. B. Liang, S. G. Louie, E. Ringe, W. Zhou, S. S. Kim, R. R. Naik, B. G. Sumpter, H. Terrones, F. N. Xia, Y. L. Wang, J. Zhu, D. Akinwande, N. Alem, J. A. Schuller, R. E. Schaak, M. Terrones, J. A. Robinson, *ACS Nano* **2015**, *9*, 11509.
- [6] G. Giovannetti, P. Khomyakov, G. Brocks, P. Kelly, J. van den Brink, *Phys. Rev. B* **2007**, *76*, 073103.
- [7] C. R. Dean, A. F. Young, I. Meric, C. Lee, L. Wang, S. Sorgenfrei, K. Watanaba, T. Taniguchi, P. Kim, K. L. Shepard, J. Hone, *Nat. Nanotechnol.* **2010**, *5*, 722.
- [8] M. Chhowalla, H. S. Shin, G. Eda, L.-J. Li, K. P. Loh, H. Zhang, *Nat. Chem.* **2013**, *5*, 263.
- [9] R. Lv, J. A. Robinson, R. E. Schaak, D. Sun, Y. Sun, T. E. Mallouk, M. Terrones, *Acc. Chem. Res.* **2015**, *48*, 56.
- [10] Y. Shi, H. Li, L.-J. Li, *Chem. Soc. Rev.* **2015**, *44*, 2744.
- [11] B. Anasori, Y. Xie, M. Beidaghi, J. Lu, B. C. Hosler, L. Hultman, P. R. C. Kent, Y. Gogotsi, M. W. Barsoum, *ACS Nano* **2015**, *9*, 9507.
- [12] H. Wang, S. L. Jiang, W. Shao, X. D. Zhang, S. C. Chen, X. X. Sun, Q. Zhang, Y. Luo, *J. Am. Chem. Soc.* **2018**, *140*, 3474.
- [13] G. Zhang, A. Chaves, S. Huang, F. Wang, Q. Xing, T. Low, H. Yan, *Sci. Adv.* **2018**, *4*, eaap9977.
- [14] Z. Meng, R. M. Stoltz, L. Mendecki, K. A. Mirica, *Chem. Rev.* **2019**, *119*, 478.
- [15] H. Liu, A. T. Neal, Z. Zhu, Z. Luo, X. F. Xu, D. Tomanek, P. D. Ye, *ACS Nano* **2014**, *8*, 4033.
- [16] X. Duan, C. Wang, A. Pan, R. Yu, X. Duan, *Chem. Soc. Rev.* **2015**, *44*, 8859.
- [17] W. Zheng, Y. Jiang, X. Hu, H. Li, Z. Zeng, X. Wang, A. Pan, *Adv. Opt. Mater.* **2018**, *6*, 1800420.
- [18] Q. Wang, K. Kalantar-Zadeh, A. Kis, J. N. Coleman, M. S. Strano, *Nat. Nanotechnol.* **2012**, *7*, 699.
- [19] L. Britnell, R. M. Ribeiro, A. Eckmann, R. Jalil, B. D. Belle, A. Mishchenko, Y.-J. Kim, R. V. Gorbachev, T. Georgiou, S. V. Morozov, A. N. Grigorenko, A. K. Geim, C. Casiraghi, A. H. Castro Neto, K. S. Novoselov, *Science* **2013**, *340*, 1311.
- [20] D. Jariwala, V. K. Sangwan, L. J. Lauhon, T. J. Marks, M. C. Hersam, *ACS Nano* **2014**, *8*, 1102.
- [21] F. H. L. Koppens, T. Mueller, Ph. Avouris, A. C. Ferrari, M. S. Vitiello, M. Polini, *Nat. Nanotechnol.* **2014**, *9*, 780.
- [22] G. Fiori, F. Bonaccorso, G. Iannaccone, T. Palacios, D. Neumaier, A. Seabaugh, S. K. Banerjee, L. Colombo, *Nat. Nanotechnol.* **2014**, *9*, 768.
- [23] X. Xu, W. Yao, D. Xiao, T. F. Heinz, *Nat. Phys.* **2014**, *10*, 343.
- [24] G. Wang, M. M. Glazov, C. Robert, T. Amand, X. Marie, B. Urbaszek, *Phys. Rev. Lett.* **2015**, *115*, 117401.
- [25] G. Berghäuser, I. Bernal-Villamil, R. Schmid, R. Scgneider, I. Niehues, P. Erhart, S. Michaelis de Vasconcellos, R. Bratschitsch, A. Knorr, E. Malic, *Nat. Commun.* **2018**, *9*, 971.
- [26] T. C. Berkelbach, M. S. Hybertsen, D. R. Reichman, *Phys. Rev. B* **2013**, *88*, 045318.
- [27] D. Y. Qiu, F. H. da Jornada, S. G. Louie, *Phys. Rev. Lett.* **2013**, *111*, 216805.
- [28] B. Radisavljevic, A. Kis, *Nat. Mater.* **2013**, *12*, 815.

- [29] P. D. Cunningham, K. M. McCreary, A. T. Hanbicki, M. Currie, B. T. Jonker, L. Michael Hayden, *J. Phys. Chem. C* **2016**, *120*, 5819.
- [30] D. Kufer, L. Nikitskiy, T. Lasanta, G. Navickaite, F. H. L. Koppens, G. Konstantatos, *Adv. Mater.* **2015**, *27*, 176.
- [31] F. K. Perkins, A. L. Friedman, E. Cobas, P. M. Campbell, G. C. Jernigan, B. T. Jonker, *Nano Lett.* **2013**, *13*, 668.
- [32] Z. Nie, R. Long, J. S. Teguh, C.-C. Huang, D. W. Hewak, E. K. L. Yeow, Z. Shen, O. V. Prezhdo, Z.-H. Loh, *J. Phys. Chem. C* **2015**, *119*, 20698.
- [33] Z. Wang, S.-S. Li, L.-W. Wang, *Phys. Rev. Lett.* **2015**, *114*, 063004.
- [34] K. F. Mak, C. G. Lee, J. Hone, J. Shan, T. F. Heinz, *Phys. Rev. Lett.* **2010**, *105*, 136805.
- [35] J. Kunstmänn, F. Mooshammer, P. Nagler, A. Chaves, F. Stein, N. Paradiso, G. Plechinger, C. Strunk, C. Schüller, G. Seifert, D. R. Reichman, T. Korn, *Nat. Phys.* **2018**, *14*, 801.
- [36] X. Luo, Y. Y. Zhao, J. Zhang, M. L. Toh, C. Kloc, Q. H. Xiong, S. Y. Quek, *Phys. Rev. B* **2013**, *88*, 195313.
- [37] X. Zhang, Q. H. Tan, J. B. Wu, W. Shi, P. H. Tan, *Nanoscale* **2016**, *8*, 6435.
- [38] W. C. Jin, P.-C. Yeh, N. Zaki, D. T. Zhang, J. T. Sadowski, A. Al-Mahboob, A. M. van der Zande, D. A. Chenet, J. I. Dadap, I. P. Herman, P. Sutter, J. Hone, R. M. Osgood, *Phys. Rev. Lett.* **2013**, *111*, 106801.
- [39] Y. Zhang, T.-R. Chang, B. Zhou, Y.-T. Cui, H. Yan, Z. Liu, F. Schmitt, J. Lee, R. Moore, Y. Chen, H. Lin, H.-T. Jeng, S.-K. Mo, Z. Hussain, A. Bansil, Z.-X. Shen, *Nat. Nanotechnol.* **2014**, *9*, 111.
- [40] L. Guo, M. Wu, T. Cao, D. M. Monahan, Y.-H. Lee, S. G. Louie, G. R. Fleming, *Nat. Phys.* **2019**, *15*, 228.
- [41] K. Hao, G. Moody, F. Wu, C. K. Dass, L. Xu, C.-H. Chen, L. Sun, M.-Y. Li, L.-J. Li, A. H. MacDonald, X. Li, *Nat. Phys.* **2016**, *12*, 677.
- [42] P. Steinleitner, P. Merkl, P. Nagler, J. Mornhinweg, C. Schüller, T. Korn, A. Chernikov, R. Huber, *Nano Lett.* **2017**, *17*, 1455.
- [43] R. Ulbricht, E. Hendry, J. Shan, T. F. Heinz, M. Bonn, *Rev. Mod. Phys.* **2011**, *83*, 543.
- [44] S. Grischkowsky, D. Keiding, M. van Exter, Ch. Fattinger, *J. Opt. Soc. Am. B* **1990**, *7*, 2006.
- [45] M. van Exter, D. Grischkowsky, *Appl. Phys. Lett.* **1990**, *56*, 1694.
- [46] N. Katzenellenbogen, D. Grischkowsky, *Appl. Phys. Lett.* **1992**, *61*, 840.
- [47] Q. Wu, X.-C. Zhang, *Appl. Phys. Lett.* **1997**, *70*, 1784.
- [48] R. A. Kaindl, F. Eickemeyer, M. Woerner, T. Elsaesser, *Appl. Phys. Lett.* **1999**, *75*, 1060.
- [49] R. Huber, A. Brodschelm, F. Tauser, A. Leitenstorfer, *Appl. Phys. Lett.* **2000**, *76*, 3191.
- [50] K. Y. Kim, A. J. Taylor, J. H. Glownia, G. Rodriguez, *Nat. Photonics* **2008**, *2*, 605.
- [51] D. Auston, *Picosecond Optoelectronic Devices*, Academic Press, New York, NY **1983**.
- [52] C. Fattinger, D. Grischkowsky, *Appl. Phys. Lett.* **1989**, *54*, 490.
- [53] B. B. Hu, X.-C. Zhang, D. H. Auston, P. R. Smith, *Appl. Phys. Lett.* **1990**, *56*, 506.
- [54] Y. Cai, I. Brener, J. Lopata, J. Wynn, L. Pfeiffer, J. B. Stark, Q. Wu, X. C. Zhang, J. F. Federici, *Appl. Phys. Lett.* **1998**, *73*, 444.
- [55] Q. Wu, X.-C. Zhang, *Appl. Phys. Lett.* **1995**, *67*, 3523.
- [56] L. Duvillaret, F. Garet, J.-L. Coutaz, *IEEE J. Sel. Top. Quantum Electron.* **1996**, *2*, 739.
- [57] S. Kar, Y. Su, R. R. Nair, A. K. Sood, *ACS Nano* **2015**, *9*, 12004.
- [58] M. C. Beard, G. M. Turner, C. A. Schmuttenmaer, *J. Phys. Chem. B* **2002**, *106*, 7146.
- [59] R. Cheville, *Terahertz Spectroscopy: Principles and Applications*, CRC, Boca Raton, FL **2008**.
- [60] Y. Lee, *Principles of Terahertz Science and Technology (Lecture Notes in Physics)* Springer Press, New York, NY **2009**.
- [61] D. Grischkowsky, *Frontiers in Nonlinear Optics*, Institute of Physics, Bristol, **1993**.
- [62] G. Grossi, G. P. Parravicini, *Solid State Physics*, Elsevier Pte. Ltd., Singapore **2015**.
- [63] S. P. Mickan, K.-S. Lee, T.-M. Lu, J. Munch, D. Abbott, X.-C. Zhang, *Microelectron. J.* **2002**, *33*, 1033.
- [64] X. Q. Zou, J. Z. Shang, J. Leaw, Z. Q. Luo, L. Y. Luo, C. L. vorakiat, L. Cheng, S. A. Cheong, H. B. Su, J.-X. Zhu, Y. P. Liu, K. P. Loh, A. H. Castro Neto, T. Yu, E. E. M. Chia, *Phys. Rev. Lett.* **2013**, *110*, 067401.
- [65] R. D. Averitt, A. J. Taylor, *J. Phys.: Condens. Matter* **2002**, *14*, R1357.
- [66] R. J. Ellingson, M. C. Beard, J. C. Johnson, P. Yu, O. I. Micic, A. J. Nozik, A. Shabaev, A. L. Efros, *Nano Lett.* **2005**, *5*, 865.
- [67] A. Pandey, P. Guyot-Sionnest, *Science* **2008**, *322*, 929.
- [68] E. Grbny, *Nature* **2015**, *522*, 274.
- [69] F. Wang, Z. Wang, L. Yin, R. Cheng, J. Wang, Y. Wen, T. A. Shifa, F. Wang, Y. Zhang, X. Zhan, J. He, *Chem. Soc. Rev.* **2018**, *47*, 6296.
- [70] F. Xia, H. Wang, D. Xiao, M. Dubey, A. Ramasubramaniam, *Nat. Photonics* **2014**, *8*, 899.
- [71] A. Radisavljevic, B. Radenovic, J. Brivio, V. Giacometti, A. Kis, *Nat. Nanotechnol.* **2011**, *6*, 147.
- [72] S. J. Haigh, A. Gholinia, R. Jalil, S. Romani, L. Britnell, D. C. Elias, K. S. Novoselov, L. A. Ponomarenko, A. K. Geim, R. Gorbachev, *Nat. Mater.* **2012**, *11*, 764.
- [73] R. F. Frindt, *J. Appl. Phys.* **1966**, *37*, 1928.
- [74] G. Vogg, M. S. Brandt, M. Stutzmann, *Adv. Mater.* **2000**, *12*, 1278.
- [75] M. Naguib, M. Kurtoglu, V. Presser, J. Lu, J. Niu, M. Heon, L. Hultman, Y. Gogotsi, M. W. Barsoum, *Adv. Mater.* **2011**, *23*, 4248.
- [76] M. Eizenberg, J. M. Blakely, *J. Chem. Phys.* **1979**, *71*, 3467.
- [77] X. Li, W. Cai, J. An, S. Kim, J. Nah, D. Yang, R. Piner, A. Velamakanni, I. Jung, E. Tutuc, S. K. Banerjee, L. Colombo, R. S. Ruoff, *Science* **2009**, *324*, 1312.
- [78] Z. Yan, J. Lin, Z. W. Peng, Z. Z. Sun, Y. Zhu, L. Li, C. S. Xiang, E. L. Samuel, C. Kittrell, J. M. Tour, *ACS Nano* **2012**, *6*, 9110.
- [79] A. Nagashima, N. Tejima, Y. Gamou, T. Kawai, C. Oshima, *Phys. Rev. Lett.* **1995**, *75*, 3918.
- [80] Y. Peng, Z. Meng, C. Zhong, J. Lu, W. Yu, Y. Jia, Y. Qian, *Chem. Lett.* **2001**, *30*, 772.
- [81] D. D. Vaughn, R. J. Patel, M. A. Hickner, R. E. Schaak, *J. Am. Chem. Soc.* **2010**, *132*, 15170.
- [82] S.-K. Mo, *Nano Convergence* **2017**, *4*, 6.
- [83] L. Kong, C. Bjelkevig, S. Gaddam, M. Zhou, Y. H. Lee, G. H. Han, H. K. Jeong, N. Wu, Z. Z. Zhang, J. Xiao, P. A. Dowben, J. A. Kelber, *J. Phys. Chem. C* **2010**, *114*, 21618.
- [84] R. M. Martin, *Electronic Structure: Basic Theory and Practical Methods*, Cambridge University Press, Cambridge **2004**.
- [85] A. H. Castro Neto, F. Guinea, N. M. R. Peres, K. S. Novoselov, A. K. Geim, *Rev. Mod. Phys.* **2009**, *81*, 109.
- [86] T. Cheiwchanwathanigij, W. R. L. Lambrecht, *Phys. Rev. B* **2012**, *85*, 205302.
- [87] J. Qiao, X. Kong, Z.-X. Hu, F. Yang, W. Ji, *Nat. Commun.* **2014**, *5*, 4475.
- [88] L. Hedin, *Phys. Rev.* **1965**, *139*, A796.
- [89] J. Heyd, G. E. Scuseria, M. Ernzerhof, *J. Chem. Phys.* **2003**, *118*, 8207.
- [90] D. Xiao, W. Yao, Q. Niu, *Phys. Rev. Lett.* **2007**, *99*, 236809.
- [91] W. Yao, D. Xiao, Q. Niu, *Phys. Rev. B* **2008**, *77*, 235406.
- [92] J. R. Schaibley, H. Yu, G. Clark, P. Rivera, J. S. Ross, K. L. Seyler, W. Yao, X. Xu, *Nat. Rev. Mater.* **2016**, *1*, 16055.
- [93] K. F. Mak, K. He, C. Lee, G. H. Lee, J. Hone, T. F. Heinz, J. Shan, *Nat. Mater.* **2013**, *12*, 207.
- [94] E. E. Salpeter, H. A. Bethe, *Phys. Rev.* **1951**, *84*, 1232.
- [95] P. Y Yu, M. Cardona, *Fundamentals of Semiconductors: Physics and Materials Properties*, Springer Press, Berlin **2010**.
- [96] H. L. Shi, H. Pan, Y.-W. Zhang, B. I. Yakobson, *Phys. Rev. B* **2013**, *87*, 155304.

- [97] S. Refaely-Abramson, D. Y. Qiu, S. G. Louie, J. B. Neaton, *Phys. Rev. Lett.* **2018**, *121*, 167402.
- [98] R. Schuster, C. Habenicht, M. Ahmad, M. Knupfer, B. Büchner, *Phys. Rev. B* **2018**, *97*, 041201.
- [99] A. Chernikov, T. C. Berkelbach, H. M. Hill, A. Rigosi, Y. L. Li, O. B. Aslan, D. R. Reichman, M. S. Hybertsen, T. F. Heinz, *Phys. Rev. Lett.* **2014**, *113*, 076802.
- [100] Z. Y. He, W. S. Xu, Y. Q. Zhou, X. C. Wang, Y. W. Sheng, Y. M. Rong, S. Q. Guo, J. Y. Zhang, J. M. Smith, J. H. Warner, *ACS Nano* **2016**, *10*, 2176.
- [101] K. Hao, J. F. Specht, P. Nagler, L. Xu, K. Tran, A. Singh, C. K. Dass, C. Schüller, T. Korn, M. Richter, A. Knorr, X. Li, G. Moody, *Nat. Commun.* **2017**, *8*, 15552.
- [102] C. Poellmann, P. Steinleitner, U. Leierseder, P. Nagler, G. Plechinger, M. Porer, R. Bratschitsch, C. Schüller, T. Korn, R. Huber, *Nat. Mater.* **2015**, *14*, 889.
- [103] P. Steinleitner, P. Merkl, A. Graf, P. Nagler, K. Watanabe, T. Taniguchi, J. Zipfel, C. Schüller, T. Korn, A. Chernikov, S. Brem, M. Selig, G. Berghäuser, E. Malic, R. Huber, *Nano Lett.* **2018**, *18*, 1402.
- [104] S. Cha, J. H. Sung, S. Sim, J. Park, H. Heo, M.-H. Jo, H. Choi, *Nat. Commun.* **2016**, *7*, 10768.
- [105] G. Berghäuser, P. Steinleitner, P. Merkl, R. Huber, A. Knorr, E. Malic, *Phys. Rev. B* **2018**, *98*, 020301.
- [106] T. Kampfrath, L. Perfetti, F. Schapper, C. Frischkorn, M. Wolf, *Phys. Rev. Lett.* **2005**, *95*, 187403.
- [107] P. A. George, J. Strait, J. Dawlaty, S. Shivaraman, M. Chandrashekhar, F. Rana, M. G. Spencer, *Nano Lett.* **2008**, *8*, 4248.
- [108] J. H. Strait, H. Wang, S. Shivaraman, V. Shields, M. Spencer, F. Rana, *Nano Lett.* **2011**, *11*, 4902.
- [109] C. Berger, Z. Song, X. Li, X. Wu, N. Brown, C. Naud, D. Mayou, T. Li, J. Hass, A. N. Marchenkov, E. H. Conrad, P. N. First, W. A. de Heer, *Science* **2006**, *312*, 1191.
- [110] M. T. Mihnev, J. R. Tolsma, C. J. Divin, D. Sun, R. Asgari, M. Polini, C. Berger, W. A. de Heer, A. H. MacDonald, T. B. Norris, *Nat. Commun.* **2015**, *6*, 8105.
- [111] D. Z. Sun, Y. Rao, G. A. Reider, G. G. Chen, Y. M. You, L. Brzin, A. R. Harutyunyan, T. F. Heinz, *Nano Lett.* **2014**, *14*, 5625.
- [112] Z. L. Wang, A. Molina-Sánchez, P. Altmann, D. Sangalli, D. De Fazio, G. Soavi, U. Sassi, F. Bottegoni, F. Ciccacci, M. Finazzi, L. Wirtz, A. C. Ferrari, A. Marini, G. Cerullo, S. Dal Conte, *Nano Lett.* **2018**, *18*, 6882.
- [113] X. C. Miao, G. W. Zhang, F. J. Wang, H. G. Yan, M. Ji, *Nano Lett.* **2018**, *18*, 3053.
- [114] X. Guo, H. Chen, X. Wen, J. Zheng, *J. Chem. Phys.* **2015**, *142*, 212447.
- [115] J. H. Strait, P. Nene, F. Rana, *Phys. Rev. B* **2014**, *90*, 245402.
- [116] X. Liu, H. Yu, Q. Ji, Z. Gao, S. Ge, J. Qiu, Z. Liu, Y. Zhang, D. Sun, *2D Mater.* **2016**, *3*, 014001.
- [117] C. He, L. Zhu, Q. Zhao, Y. Huang, Z. Yao, W. Du, Y. He, S. Zhang, X. Xu, *Adv. Opt. Mater.* **2018**, *6*, 1800290.
- [118] N. M. R. Peres, F. Guinea, A. H. Castro Neto, *Phys. Rev. B* **2006**, *73*, 125411.
- [119] I. Maeng, S. Lim, S. J. Chae, Y. H. Lee, H. Choi, J.-H. Son, *Nano Lett.* **2012**, *12*, 551.
- [120] J. D. Buron, F. Pizzocchero, B. S. Jessen, T. J. Booth, P. F. Nielsen, O. Hansen, M. Hilke, E. Whiteway, P. U. Jepsen, P. Bggild, D. H. Petersen, *Nano Lett.* **2014**, *14*, 6348.
- [121] K. F. Mak, M. Y. Sfeir, Y. Wu, C. H. Lui, J. A. Misewich, T. F. Heinz, *Phys. Rev. Lett.* **2008**, *101*, 196405.
- [122] P. Avouris, *Nano Lett.* **2010**, *10*, 4285.
- [123] J. Lu, H. Liu, J. Sun, *Nanotechnology* **2017**, *28*, 464001.
- [124] J. Lu, H. Liu, *Opt. Commun.* **2018**, *406*, 24.
- [125] G. Jnawali, Y. Rao, H. Yan, T. F. Heinz, *Nano Lett.* **2013**, *13*, 524.
- [126] K. J. Tielrooij, J. C. W. Song, S. A. Jensen, A. Centeno, A. Pesquera, A. Zurutuza Elorza, M. Bonn, L. S. Leviton, F. H. L. Koppens, *Nat. Phys.* **2013**, *9*, 248.
- [127] A. J. Frenzel, C. H. Lui, W. Fang, N. L. Nair, P. K. Herring, P. Jarillo-Herrero, J. Kong, N. Gedik, *Appl. Phys. Lett.* **2013**, *102*, 113111.
- [128] C. J. Docherty, P. Parkinson, H. J. Joyce, M.-H. Chiu, C.-H. Chen, M.-Y. Lee, L.-J. Li, L. M. Herz, M. B. Johnston, *ACS Nano* **2014**, *8*, 11147.
- [129] X. Xing, L. Zhao, Z. Zhang, X. K. Liu, K. L. Zhang, Y. Yu, X. Lin, H. Y. Chen, J. Q. Chen, Z. M. Jin, J. H. Xu, G.-H. Ma, *J. Phys. Chem. C* **2017**, *121*, 20451.
- [130] C. H. Lui, A. J. Frenzel, D. V. Pilon, Y.-H. Lee, X. Ling, G. M. Akselrod, J. Kong, N. Gedik, *Phys. Rev. Lett.* **2014**, *113*, 166801.
- [131] Y. Zhan, Z. Liu, S. Najmaei, P. M. Ajayan, J. Lou, *Small* **2012**, *8*, 966.
- [132] X.-Q. Lee, Y.-H. Zhang, W. Zhang, M.-T. Chang, C.-T. Lin, K.-D. Chang, Y.-C. Yu, J. T.-W. Wang, C.-S. Chang, L.-J. Li, T.-W. Lin, *Adv. Mater.* **2012**, *24*, 2320.
- [133] D. Sanvitto, F. Pulizzi, A. J. Shields, P. C. M. Christianen, S. N. Holmes, M. Y. Simmons, D. A. Ritchie, J. C. Maan, M. Pepper, *Science* **2001**, *294*, 837.